A Unified Charge Storage Mechanism to Rationalize the Electrochemical Behavior of Quinone-Based Organic Electrodes in Aqueous Rechargeable Batteries

Wenkang Wang, Véronique Balland, Mathieu Branca, Benoît Limoges

A unified charge storage mechanism to rationalize the electrochemical behavior of quinone-based organic electrodes in aqueous rechargeable batteries

Wenkang Wang, Véronique Balland, Mathieu Branca and Benoît Limoges**
Université Paris Cité, CNRS, Laboratoire d'Electrochimie Moléculaire, F-75013 Paris, France.
E-mails: mathieu.branca@u-paris.fr ; limoges@u-paris.fr

Keywords: organic electrode, aqueous battery, quinone electrochemistry, charge storage mechanism, chloranil, duroquinone, proton insertion, proton-coupled electron transfer, square scheme, phase transition

Abstract

Due to their eco-sustainability and versatility, organic electrodes are promising candidates for large-scale energy storage in rechargeable aqueous batteries. This is notably the case of aqueous hybrid batteries that pair the low voltage of a zinc anode with the high voltage of a quinone-based (or analogue of quinone-based) organic cathode. However, the mechanisms governing their charge-discharge cycles remain poorly understood and are even a matter of debate and controversy. No consensus exists on the charge carrier in mild aqueous electrolytes, especially when working in an electrolyte containing a multivalent metal cation such as Zn^{2+}. In this study, we comprehensively investigate the electrochemical reactivity of two model quinones, chloranil and duroquinone, either diluted in solution or incorporated into carbon-based composite electrodes. We demonstrate that a common nine-member square scheme proton-coupled electron transfer mechanism allows us to fully describe and rationalize their electrochemical behavior in relation to the pH and chemical composition of the aqueous electrolyte. Additionally, we highlight the crucial role played by the pK_as associated with the reduced states of quinones in determining the nature of the charge carrier that compensates for the negative charges reversibly injected in the active material. Finally, contrary to the widely reported findings for Zn/organic batteries, we unequivocally establish that the predominant solid-state charge carriers in Zn^{2+}-based mild aqueous electrolytes are not multivalent Zn^{2+}

cations but rather protons supplied by the weakly acidic hexaaqua metal ions (*i.e.*, $[Zn(H_2O)_6]^{2+}$]).

1 Introduction

In recent years, there has been a tremendous resurgence of interest in aqueous rechargeable batteries because of the role they could play in the energy transition and, in particular, for their potential to meet the growing demand for large-scale storage of electricity generated by renewable energies.[1-2] Compared to other energy storage technologies, aqueous batteries offer multiple advantages such as reasonable energy densities, high power densities, high robustness, safety, low production and maintenance costs, and the ability to be mass-produced from abundant materials with low environmental impact. In addition, their eco-sustainability and recyclability can be further enhanced if some of the metal- or metal oxide-based active materials commonly employed in aqueous batteries are substituted by redox-active organic materials.[4-6] This is for instance the case of zinc-organic batteries, which have recently emerged as a promising alternative class of rechargeable aqueous hybrid batteries.[7-11] These rechargeable batteries combine the advantages of an inexpensive and environmentally-friendly zinc anode, exchanging 2 e^- per zinc atom by electrodissolution/electrodeposition at a low potential (-0.763 V vs. SHE), with those of a low-cost and eco-sustainable redox-active organic cathode, also exchanging 2 e^- per redox center but at a high potential through a reversible electrochemical reaction coupled to charge compensation *via* the soluble charge carriers. Hence, many recent works have shown that aromatic compounds belonging to the quinone family and their analogues (*i.e.*, n-type conjugated carbonyl- or imine-containing compounds[4, 9, 12]) can lead to positive organic electrodes with charge-storage performances competitive with those of inorganic metal oxide-based materials in aqueous electrolytes.[7, 8, 13]

However, the charge storage mechanism of these electrodes in Zn^{2+}-based aqueous electrolytes still remains unclear. Three different charge storage mechanisms were indeed proposed (Scheme 1). The most frequently reported is assumed to follow the reversible coordination of Zn^{2+} ions to the negatively charged redox-active centers of reduced organic materials. This has been reported for the first time in 2018, in three independent papers involving different quinone-based electrodes (*i.e.* a calix[4]quinone,[14] the tetrachloro-1,4-benzoquinone,[15] and a pyrene-4,5,9,10-tetraone (PTO)[16]) in aqueous electrolytes (mildly acidic) made of a few molars of $ZnSO_4$ or $Zn(CF_3SO_3)_2$. This mechanism of reversible charge compensation through coordination of multivalent metal cations (mainly Zn^{2+} but also Mg^{2+} [17], Al^{3+} [18], and even Ca^{2+} [19]) was thereafter taken up for a wide range of either n-type conjugated carbonyl- or imine-containing compound.[5, 7, 12] The second reported mechanism, mostly for quinone- or quinone analog-based electrodes, is the reversible storage of protons.[13] This is a fairly obvious mechanism when the electrolyte is a strong acid like H_2SO_4,[17, 20-25] but it is much less clear when the aqueous electrolyte is mildly acidic. Indeed, a majority of groups propose the reversible co-uptake of H^+ and Zn^{2+} when working in a mild acidic aqueous $ZnSO_4$ electrolyte,[26-32] while a few others suggest a charge storage exclusively based or largely dominated by the reversible uptake of protons, and this either with carbonyl-[33, 34] or imine-based redox active organic electrodes.[35, 36] There are even controversial results in literature where different charge storage mechanisms are proposed for a same quinone moiety (the PTO moiety is a good example[16, 29, 37-39]). Furthermore, the question of the origin of protons,

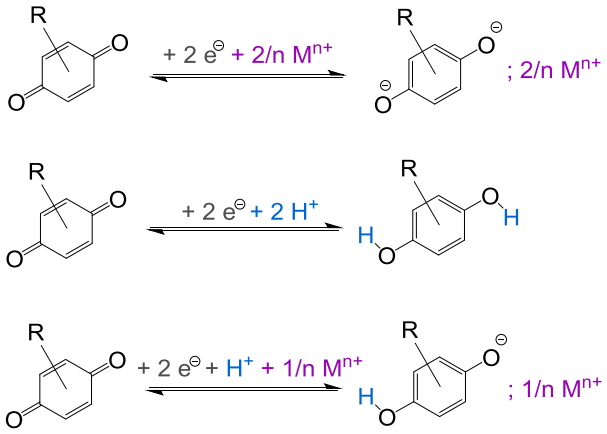

Scheme 1. Three currently proposed charge storage mechanisms of quinone-based organic electrodes in aqueous rechargeable batteries, where M^{n+} denotes the multivalent metal cation present in the electrolyte.

when considered as solid-state charge carriers, remains largely unresolved,[34, 35] leading some groups to propose that protons originate from the solvent water *via* its self-ionization,[36] which, as we will show below, is incorrect when working in the presence of Zn^{2+} in the electrolyte.

All these elements underline the lack of fundamental understanding in the charge storage mechanism of aqueous Zn-organic batteries, with an absence of consensus on a reaction scheme allowing to explain why and when the negative charges of an n-type organic electrode can be reversibly and preferentially compensated by Zn^{2+} cations rather than protons and *vice versa*. We propose here to fill this gap with the investigation of two different model quinone-based electrodes, namely tetrachloro-1,4-benzoquinone- (or chloranil) and tetramethyl-1,4-benzoquinone-based (or duroquinone) composite electrodes, that we have characterized in detail either by cyclic voltammetry or galvanometric cycling experiments in different pHs and electrolyte compositions. As it will be shown, a unique reaction scheme can be used to fully explain and rationalize the electrochemical charge-discharge behavior of these electrodes in a wide range of aqueous electrolytes (either buffered or unbuffered) and pHs, including the transition from a proton- to a cation-coupled charge storage mechanism.

2 Results and Discussion

2.1 Electrochemistry of chloranil and duroquinone in aqueous buffered electrolytes

Before characterizing the composite organic electrodes made of chloranil (or tetrachloro-1,4-benzoquinone) or duroquinone (or tetramethyl-1,4-benzoquinone), we first examined, by cyclic voltammetry (CV), the electrochemical behavior of these two redox-active molecules diluted (0.1 mM) in buffered aqueous electrolytes at different pHs ranging from 0 to 12 (using a standard three-electrode cell with a glassy carbon electrode as the working electrode). The CVs gathered in Figures 1a and 1e are in agreement with the well-known 2 e^-, 2 H^+ electrochemical reduction of quinone (Q) into hydroquinone (QH_2) (eq. 1), leading over a wide pH range to a single reversible 2 e^- faradaic wave centered on a $E_{1/2}$ potential (taken as the average of the cathodic and anodic peak potentials, *i.e.* $E_{p,red}$ and $E_{p,ox,}$ respectively).[40, 41] As expected, it varies for both quinones of ~ -59 mV per pH unit (in agreement with a 2 e^-, 2 H^+ transfer) over a wide pH range (Figures 1c and 1g).[42]

$$Q + 2\,H^+ + 2\,e^- \underset{}{\overset{E^0_{app}}{\rightleftharpoons}} QH_2 \qquad (1)$$

This pH dependency is direct evidence that protons participate to the electrochemical reaction (the protons being provided by the acid form of the buffer, while the buffer also helps to maintain the pH constant at the electrode interface during the whole electrochemical process). Interestingly, for pHs > 6.5, the single 2 e^-, 2 H^+ reversible wave of chloranil splits into two distinct reversible waves of lower intensity, the first one being pH-independent and the second varying by -59 mV/pH up to pH 8.5, after which it also becomes pH-independent. If we consider that each reduction wave is the resultant of two sequential one-electron transfer

processes, the first wave must therefore be a pure one-electron transfer reaction wherein Q is reduced to $Q^{\bullet-}$, while the second must involve the transfer of one electron and one proton to produce QH^-, and this until the pH is sufficiently basic so that the second wave no longer involves a proton transfer (leading thus to a second horizontal plot on the *E*-pH diagram of Figure 1c). As a result, at pH > 8.5, the chloranil reduction pathway can be described by two sequential one-electron transfer reactions without coupled protonation (eqs. 2 and 3), leading first to the semiquinone radical intermediate, $Q^{\bullet-}$, followed then by formation of the doubly deprotonated hydroquinone Q^{2-} (where E_1^0 and E_2^0 are the standard potentials of the redox couple $Q/Q^{\bullet-}$ and Q/Q^{2-},

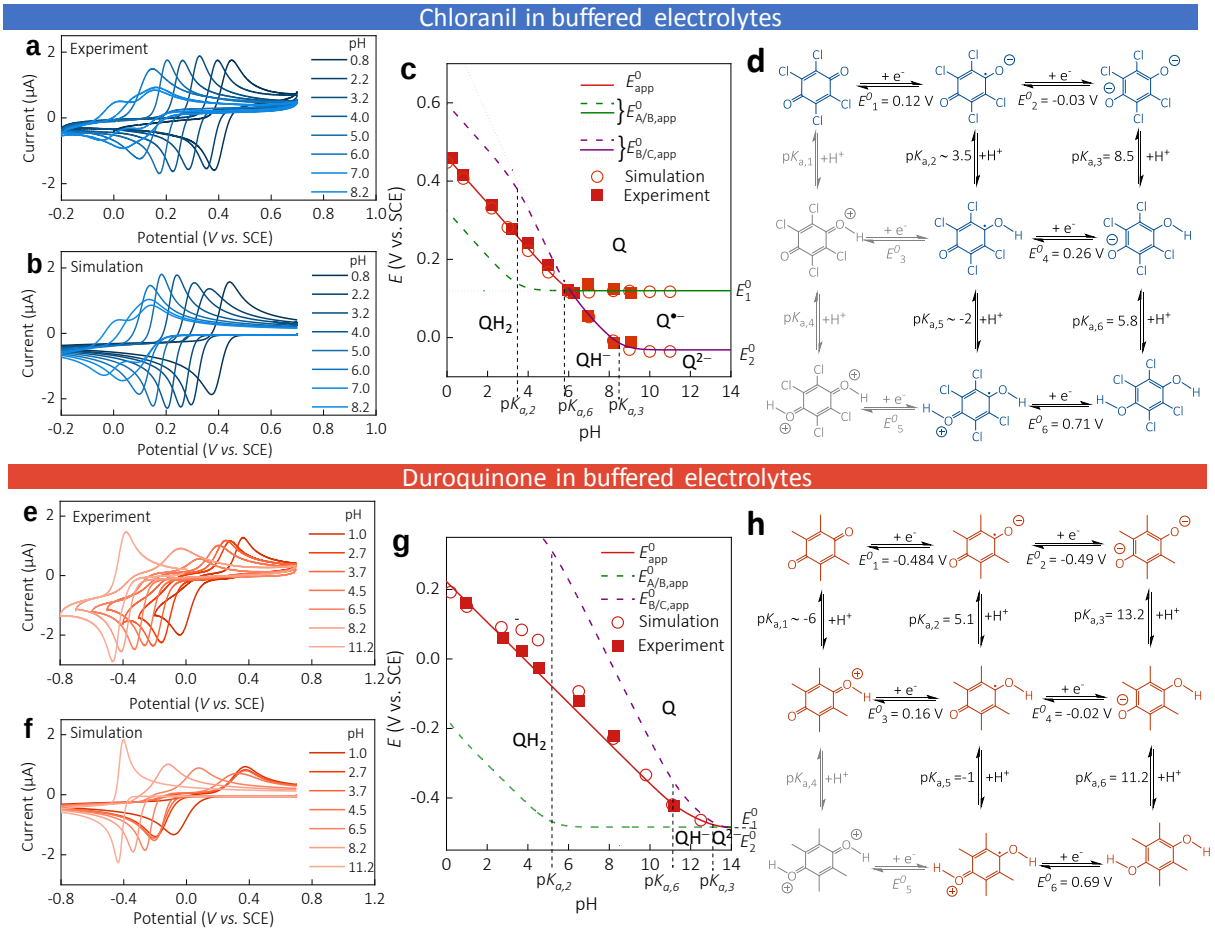

Figure 1. CVs (v = 30 mV s^{-1}) of 0.1 mM (a, b) chloranil or (e, f) duroquinone in buffered aqueous solutions at different pHs (the pH values are indicated on the graphs). The experimental (a, e) and simulated (b, f) results are plotted separately. (c, g) E-pH diagrams of (c) chloranil and (g) duroquinone, in which red solid square and red empty dot symbols are the experimental and simulated $E_{1/2}$ (*i.e.*, average of $E_{p,red}$ and $E_{p,ox}$) extracted from CVs, and solid and dashed lines are the theoretical plots of (green) $E^{0}_{A/B,app}$, (purple) $E^{0}_{B/C,app}$, and (red) E^{0}_{app} calculated from eqs. 5, 6, and 9, respectively, and using the pK_as and potential values reported in schemes d and h. The short dotted green and purple lines in graph c were obtained from eqs. 5 and 6 in which the p$K_{a,1}$ and p$K_{a,4}$ values were considered as sufficiently acidic for being neglected. (d, h) Nine-membered square schemes of (d) chloranil and (h) duroquinone with the known and estimated thermodynamic parameters (potentials are *vs.* SCE). Reactions that can be considered as negligible because of their too high potential values or very acidic pK_as appear in light gray.

respectively, and the negative charges being compensated by the X^+ cations present in solution).

$$Q + e^- + X^+ \overset{E^0_1}{\rightleftharpoons} Q^{\bullet -}; X^+ \quad (2)$$

$$Q^{\bullet -}; X^+ + e^- + X^+ \overset{E^0_2}{\rightleftharpoons} Q^{2-}; 2\,X^+ \quad (3)$$

Values of E_1^0 = 0.12 V and E_2^0 = -0.03 V (*vs.* SCE) can thus be directly read from the two horizontal lines fitted to the data in Figure 1c (solid green and purple lines). One can notice that the E_1^0 value agrees with the one previously reported for chloranil.[43]

The two well-separated reversible waves observed for chloranil at pH > 7.0 is rather unusual for a quinone in an aqueous media.[44] This separation of the two one-electron reductions implies that the semiquinone intermediate $Q^{\bullet -}$ is thermodynamically stable, a stability that can be quantified through the following disproportionation/comproportionation equilibrium:

$$2\ Q^{\bullet -};\ X^+ \underset{\leftarrow}{\overset{K_{dis}}{\rightleftharpoons}} Q + Q^{2-};\ 2\ X^+ \qquad (4)$$

with $K_{dis} = e^{-F/RT\left(E_1^0 - E_2^0\right)}$ (a value of $K_{dis} \approx 0.0025$ can thus be calculated). This singular behavior can be attributed to the weak basicity of the reduced quinone, a consequence of the strong electron-withdrawing effect of the four chloro substituents, leading to pK_as of 5.6 and 8.2, respectively, for the QH_2/QH^- and QH^-/Q^{2-} acid/base couples.[43] The consequence of this weak basicity means that at high pHs, the predominant species Q^{2-} is only weakly stabilized by hydrogen bonding with water. This is in contrasts to what is generally encountered with more basic benzohydroquinones which, on account of their high pK_as, are strongly stabilized in their Q^{2-} state by their strong hydrogen bonding with water.[45-47] This hydrogen bonding stabilization has the consequence of shifting E_2^0 (and also, to a lesser extent, E_1^0) towards positive values, which, for numerous quinones, leads to a potential inversion with $E_2^0 > E_1^0$ (leading in CV to a single two-electron wave, even at very basic pHs where Q^{2-} is the predominant species).[45-47] This is notably the case of duroquinone whose pK_as of QH_2 are 11.2 and 13.2.[48] As a result, a single reversible 2 e^- wave is obtained in CV over the whole pH range (Figures 1e and 1g).[40, 49] Independently of rendering Q^{2-} much more basic, the electron-donating character of the four methyl groups also contributes to shifting the E_{app}^0 to lower potentials than chloranil (by ~-200 mV).

Because of the importance of quinones in many fields, their proton-coupled electron transfer (PCET) mechanisms have been widely investigated, both theoretically and experimentally.[50, 51] Their mechanism can be interpreted on the basis of the general nine-member square scheme presented in Scheme 2, where the horizontal reactions correspond to electron transfers (ETs) and the vertical ones to proton exchanges.

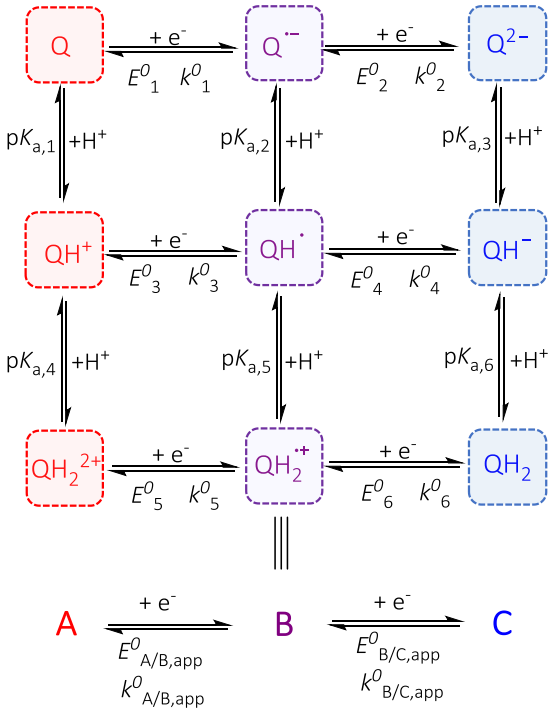

Scheme 2. Nine-membered square scheme

The mechanistic pathway is thus heavily dependent on the pK_a of the redox-active species as well as on the local pH environment. Laviron has demonstrated[49, 52] that under conditions where (*i*) protonations are at equilibrium (which is assumed to be the case in buffered aqueous media), (*ii*) electrochemical transfer coefficients (*i.e.*, α) are 0.5, and (*iii*) disproportionation and dimerization reactions are absent, the nine-member square scheme can be reduced to a simple mechanism made of two successive one-electron transfer reactions (Scheme 2), each characterized by an apparent rate constant $k^0_{A/B,app}$ and $k^0_{B/C,app}$, and an apparent standard

potential $E^{0}_{\mathrm{A/B,app}}$ and $E^{0}_{\mathrm{B/C,app}}$, respectively. The expressions of these apparent standard potentials are recalled below.

$$E^{0}_{\mathrm{A/B,app}} = E^{0}_{3} + \frac{RT}{F}\ln\left(\frac{\frac{K_{a,2}}{[\mathrm{H}^+]} + 1 + \frac{[\mathrm{H}^+]}{K_{a,5}}}{\frac{K_{a,1}}{[\mathrm{H}^+]} + 1 + \frac{[\mathrm{H}^+]}{K_{a,4}}}\right) \quad (5)$$

$$E^{0}_{\mathrm{B/C,app}} = E^{0}_{4} + \frac{RT}{F}\ln\left(\frac{\frac{K_{a,3}}{[\mathrm{H}^+]} + 1 + \frac{[\mathrm{H}^+]}{K_{a,6}}}{\frac{K_{a,2}}{[\mathrm{H}^+]} + 1 + \frac{[\mathrm{H}^+]}{K_{a,5}}}\right) \quad (6)$$

wherein E^{0}_{3} and E^{0}_{4} are linked to E^{0}_{1} and E^{0}_{2} through the following thermodynamic relationships:

$$E^{0}_{3} = E^{0}_{1} + \frac{2.3RT}{F}\left(\mathrm{p}K_{a,2} - \mathrm{p}K_{a,1}\right) \quad (7)$$

$$E^{0}_{4} = E^{0}_{2} + \frac{2.3RT}{F}\left(\mathrm{p}K_{a,3} - \mathrm{p}K_{a,2}\right) \quad (8)$$

From eqs. 5 and 6, the apparent equilibrium potential can be easily obtained:

$$E^{0}_{\mathrm{app}} = (E^{0}_{\mathrm{A/B,app}} + E^{0}_{\mathrm{B/C,app}})/2 \quad (9)$$

while the other potentials can be calculated from the following additional thermodynamic relationships:

$$E^{0}_{5} = E^{0}_{3} + \frac{2.3RT}{F}\left(\mathrm{p}K_{a,5} - \mathrm{p}K_{a,4}\right) \quad (10)$$

$$E^{0}_{6} = E^{0}_{4} + \frac{2.3RT}{F}\left(\mathrm{p}K_{a,6} - \mathrm{p}K_{a,5}\right) \quad (11)$$

Provided that a minimal set of pK_as values and apparent standard potentials are known, one can draw, using eqs. 5, 6 and 9, the *E*-pH diagram (or Pourbaix diagram) of chloranil and duroquinone (dashed/plain green, dashed/plain purple and solid red curves, respectively, in

Figures 1c and 1g) (the thermodynamic parameters used to plot these theoretical curves are gathered in Figures 1d and 1h – the pK_as and E^0s of duroquinone were taken from literature,[48, 53-57] while for chloranil some constants were from literature[43] and other have been adjusted to give the best fit to the experimental data, *vide infra*). In the case of chloranil, in a first approximation we have considered that the unknown pK_as of the protonated quinones and semiquinones (*i.e.* p$K_{a,1}$, p$K_{a,2}$, p$K_{a,4}$ and p$K_{a,5}$) are acidic enough for their contributions in eqs 5, 6, or 9 to be negligible. Under these conditions, only the thermodynamic parameters p$K_{a,3}$, p$K_{a,6}$, E_1^0 and E_2^0 count. By adjusting these parameters so that eqs. 5, 6 and 9 best fit the experimental data, we were able to plot, respectively, the dotted/solid green, dotted/solid purple and solid red curves in Figure 1c using the following set of values: p$K_{a,3}$ = 8.5, p$K_{a,6}$ = 5.8, E_1^0 = 0.12 V and E_2^0 = -0.03 V.

The *E*-pH diagrams plotted in Figures 1c and 1g are useful for visualizing the pH range where the overall 2 e^-, 2 H^+ reaction takes place (with a E_{app}^0 varying by -59 mV/pH unit – solid red plots). In the case of duroquinone, we can see that it extends over the entire pH range investigated, while for chloranil it is only effective within the pH range 0 to ~7. From the *E*-pH diagram of chloranil, we can also easily discern the pH at which the single reversible 2 e^- transfer splits into two reversible 1 e^- transfers.

To complete our analysis and confirm the relevance of the proposed mechanisms, digital simulations of the CVs were performed (see the Supporting Information and Table S1 for details on simulations). For such a purpose, the square-scheme mechanisms with their thermodynamic parameters (Figures 1d and 1h) were considered to take place at an electrode boundary with no homogeneous reactions in solution (*i.e.*, the contribution of homogeneous disproportionation/comproportionation reactions were assumed negligible[58]), while a 1D-semi-infinite linear diffusion normal to the electrode was set for the species in solution. The standard Butler-Volmer formalism was also applied to all elementary electrochemical

reactions (with α values of 0.5), with the assumption of relatively fast and identical heterogeneous ET rate constants for chloranil (set to k^0 = 1 cm/s),[59] while for duroquinone some of the heterogeneous ET rate constants were adjusted in order to better fit the experimental CVs (notably k^0_3, k^0_4, k^0_6, which were set to 300, 30, and 2 cm/s, respectively – It is to note that these values are not far from those previously determined for analogous benzoquinones[60-62]). For modeling the protonation steps, all possible acid/base equilibriums were considered (by taking into account all proton donor/acceptor couples present in the electrolyte, *i.e.*, H_3O^+/H_2O, H_2O/OH^-, and AH/A^-, where AH and A^- are the conjugate acid and base of the buffer). Moreover, all protonation rates were assumed identical and close to the diffusion limit (values ranging from 10^{10} to 10^{11} $M^{-1}\cdot s^{-1}$ were used), while the pH was set by adjusting the concentrations of the acid and base forms of the buffer.[63]

The simulated CVs for both quinones at different pHs (Figures 1b and 1f) reproduce quite well the experimental ones (Figures 1a and 1e). In the case of chloranil, the best matches were obtained by roughly adjusting the p$K_{a,2}$ and p$K_{a,5}$ values to ~ 3.5 and ~ -2, respectively. Compared to duroquinone (p$K_{a,2}$ = 5.1 and p$K_{a,5}$ = -1.1), these pK_as are quite reasonable considering the electron withdrawing effects of the 4 chloro substituents of chloranil (correlating well with the pK_as we can estimate from the Hammett's sigma constants of -Cl *vs.* $-CH_3$ substituents[61, 64]). Also, a good match between experimental and simulated data was obtained by reporting the $E_{1/2}$ values inferred from the simulated CVs on the *E*-pH diagram (empty dot symbols in Figures 1c and 1g). These results finally underline the relevance of the square scheme mechanisms in Figures 1d and 1h, including the associated thermodynamic parameters.

2.2 Electrochemistry of chloranil and duroquinone composite electrodes in buffered aqueous electrolytes

The next step was to determine to what extent the above PCET mechanisms persist once quinones are incorporated within the composite matrix of solid electrodes (prepared from a slurry consisting of 60% active material, 10% polymer binder, and 30% carbon powder – see Experimental Section for details). An interesting property of chloranil and duroquinone is that they are both very sparingly soluble in water, leading to relatively stable composite electrodes in aqueous electrolytes.[15, 65]

The graphs a and b in Figure 2 show a representative set of CVs recorded at Ketjenblack carbon-based chloranil and duroquinone electrodes (in a three-electrode setup) in 0.5 M buffered electrolytes at three different mild acidic pHs. As in homogeneous solutions, the CVs display a pair of reversible reduction and oxidation peaks, characteristic of the reversible 2 e^-, 2 H^+ reduction of Q into QH_2. For both quinones, the areas of the oxidation and reduction peaks are almost identical, demonstrating a high degree of chemical reversibility. The reversible waves are also centered on $E_{1/2}$ that are close to those previously obtained from solution at the same pHs (with a same Nernstian shift of -59 mV/pH), exhibiting only a slight overall offset towards negative potentials (see the insets of Figures 2a and 2b). This pH dependency clearly indicates for both quinones the persistence of the PCET process in the solid phase. However, the shape of the voltammetric peaks differs considerably from those obtained with dissolved quinones, suggesting a thin-layer type response due to the absence of a "tail" in the faradaic peak currents (the latter dropping to almost zero). Another striking difference with the chloranil is the much larger peak-to-peak potential separation (ΔE_p) than in solution (ΔE_p ~200 mV *vs.* ~40 mV in solution) and this despite the slower scan rate. On the other hand, for duroquinone, the apparent reversibility is in contrast clearly improved

compared to the homogeneous solution at the same pHs. One possible explanation for the high ΔE_p of chloranil lies in the establishment of a concentration polarization at the electrode interface. This can occur if the supply of proton donors/acceptors is insufficient to sustain the reversible local consumption of 2 H^+ per quinone molecule, resulting in the formation of pH gradients in the vicinity of the electrode and hence in voltage hysteresis. To test this hypothesis, the influence of the buffer concentration at a constant pH value on the CVs of chloranil electrode was examined. As shown in Figure 2c, decreasing the buffer concentration leads to an increase in ΔE_p and, at a same time, a slight decrease in peak areas. These behaviors are well consistent with an insufficient supply of proton donors/acceptors at low buffer concentration. Increasing the buffer concentration and decreasing the scan rate thus helps to mitigate this effect. A similar behavior is also observed in a non-buffered electrolyte containing HCl. Indeed, the CVs in Figure 2d demonstrate that by increasing the HCl concentration, ΔE_p becomes smaller and tends toward a constant value. Here, the reversible waves are also shifted by -59 mV/pH unit (see the inset of Figure 2d), a behavior which fully agrees with the pH-dependent Nernst equation inferred from reaction 1, *i.e.*:

$$E = E^{0}_{Q/QH_2,\,pH=0} - 2.302\frac{RT}{F}\,pH \qquad (12)$$

What remains however intriguing is that even at high buffer or acid concentrations and slow scan rates (Figure 2e), a large ΔE_p is still observed, converging, whatever the pH, to an important non-null value at slow scan rates (Figure 2h). Concentration polarization is therefore not the sole explanation for the large ΔE_p. The fact that it converges to a constant value at slow scan rates suggest that there is a need to overcome a threshold activation barrier to trigger the electrochemical reaction. Interestingly, this seems to correlate with the abrupt increase of the faradic current (cathodic or anodic) once an overvoltage threshold is passed, leading to singular discontinuities at the foot of the reduction and oxidation peaks on the CVs

(Figure 2e and also Figure S1). All these elements are the tell-tale signs of a reversible solid-solid phase transformation (or phase transition) of chloranil during its reversible PCET reduction (where the quinone probably undergoes a solid-state two-phase separation), the rate of which is probably controlled by a nucleation and growth process.[66]

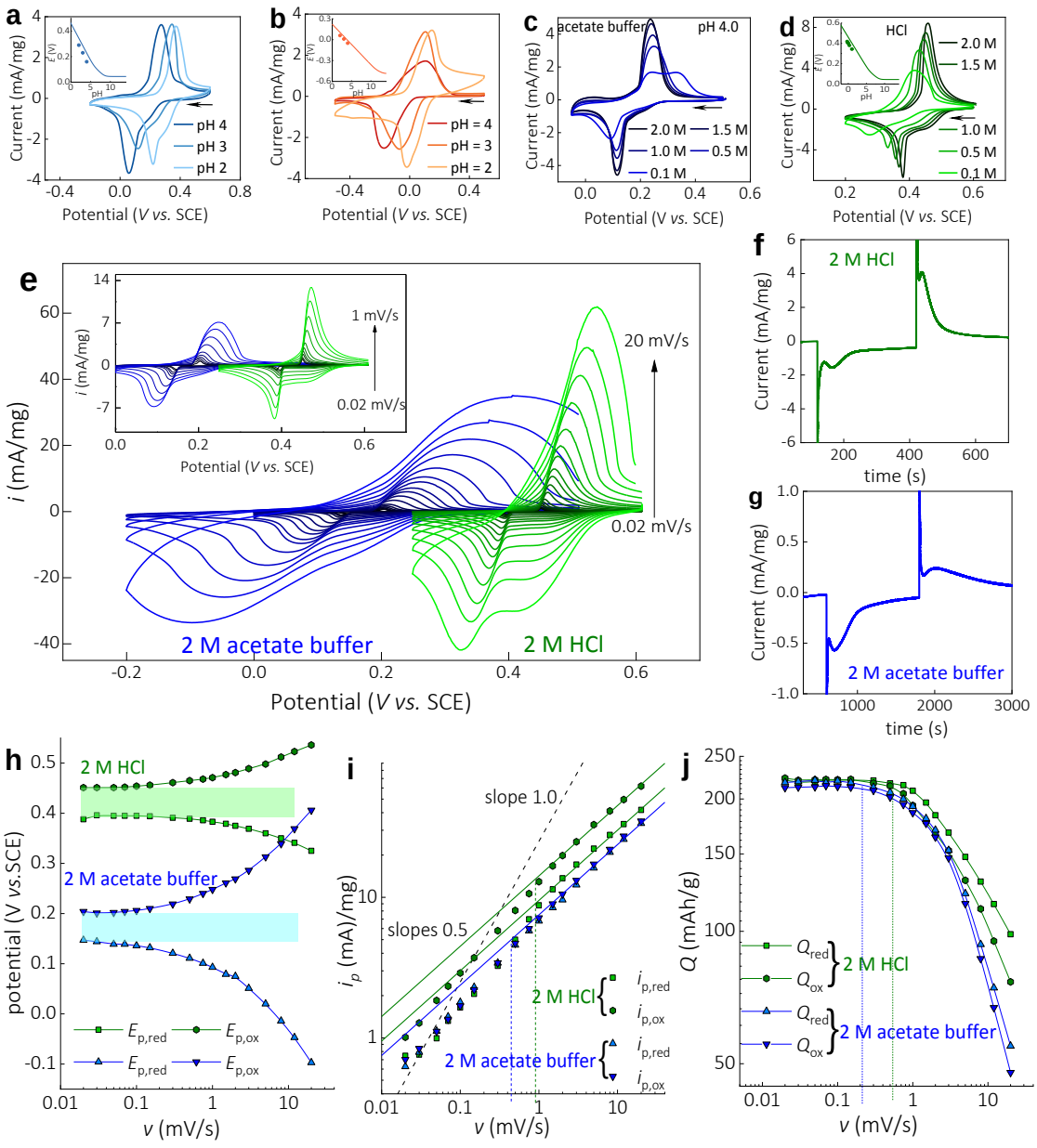

Figure 2. CVs (v = 1 mV s^{-1}) of Ketjenblack EC-300J carbon-based (a) chloranil and (b) duroquinone electrodes recorded in 0.5 M buffered aqueous electrolytes at three different pHs (the pH values are indicated on the graphs). (c) CVs (v = 1 mV s^{-1}) of a Ketjenblack EC-300J carbon-based chloranil electrode recorded in aqueous acetate buffers (pH 4.0) of different concentrations (see the graph legend). (d) CVs (v = 1 mV s^{-1}) of a Ketjenblack EC-300J carbon-based chloranil electrode in HCl electrolyte of different concentrations and so pHs (see the graph legend). Insets in a, b and d: (solid dots) $E_{1/2}$ recovered from the CVs as a function of pH and (solid curves) theoretical E^{0}_{app} -pH plots of the quinones recovered from homogeneous solution (*i.e.*, same than the red curves in Figure 1). All currents were normalized to the mass of active material. (e) CVs recorded at Ketjenblack EC-300J carbon-based chloranil electrodes in a (blue) 2 M acetate buffer (pH 4.0) and a (green) 2 M

HCl (pH ~ -0.3) at the following different scan rates: (from the darkest to lightest blue or green curves) v = 0.02, 0.03, 0.05, 0.07, 0.1, 0.15, 0.3, 0.5, 0.75, 1, 1.5, 2, 3, 5, 8, 12, and 20 mV/s (inset in graph e is a zoom on the CVs performed at the slowest scan rates). The currents were all normalized to the mass of active material. (f, g) Double-potential-step chronoamperograms recorded at chloranil electrodes in (f) 2 M HCl and (g) 2 M acetate buffer (pH 4.0). The potential (*vs.* SCE) was stepped (f) from open-circuit to +0.425 V for 2 min, then to +0.400 V for 5 min, and finally to +0.450 V for 5 min, and (g) from open-circuit to +0.180 V for 2 min, then to +0.160 V for 5 min, and finally to + 0.200 for 5 min. (h) Semi-log plot of the reduction ($E_{p,red}$) and oxidation ($E_{p,ox}$) peak potentials (recovered from the CVs in e) as a function of v. (i) Log-log plot of the CV peak currents in graph e as a function of v. The straight lines are the fits of $i_p = f(v)$ (*i.e.* slope 1.0, dashed line) or $i_p = f(\sqrt{v})$ (*i.e.* slope 0.5, solid lines) to the data. (j) Log-log plot of the charges integrated from the reduction (Q_{red}) and oxidation (Q_{ox}) peak currents in graph e as a function of v. The vertical dashed lines in graphs i and j indicate the transition from a diffusion-controlled to a surface-controlled process.

Further evidence for a nucleation and growth process is provided by the double-potential-step chronoamperometry experiments shown in Figures 2f and 2g. Indeed, the two successive potential steps exhibit transient current responses which do not follow the classical asymptotic decrease of faradaic current,[67] but instead show, after a rapid decay of capacitive current (corresponding to the vertical spikes at the very beginning of the current responses), the formation of a more or less pronounced faradaic peak after the application of each step potential (see also the additional results provided in Figure S2). Such a current evolution is characteristic of nucleation and growth kinetics,[66] which moreover is observed here depending on the nature and/or pH of the electrolyte (the peak sets up much faster in HCl than in acetate buffer). It is to note that, in contrast to inorganic insertion materials,[68-72] phase transitions with nucleation and growth kinetics were only scarcely reported for organic electrode materials,[15, 66, 73] and even more rarely unambiguously demonstrated.[74]

The additional information we extracted from the CVs is the cathodic and anodic peak currents ($i_{p,red}$ and $i_{p,ox}$) as a function of scan rate, represented on a log-log scale in Figure 2i. In both acetate buffer and HCl electrolytes, above *ca.* 0.4 and 1 mV/s, respectively, $i_{p,red}$ and $i_{p,ox}$ scale linearly with $\sqrt{v}$ (*i.e.*, slope of 0.5 in Figure 2i), while below they scale neither to $\sqrt{v}$ or v but in between (*i.e.*, slope varying from 0.6 to 0.7 in Figure 2i). This behavior differs from what is expected when moving from a semi-infinite diffusion-controlled process (proportional to $\sqrt{v}$) to a finite diffusion-free process (proportional to v) under thin-layer CV conditions. In order to ascertain from which threshold scan rate all electroactive molecules

contained within the thin-film are reduced or oxidized, the peak currents were integrated and the resulting charges Q_{red} and Q_{ox} plotted as a function of v in Figure 2j (on a log-log scale). From this graph, it can be established that the quasi-equal charges Q_{red} and Q_{ox}, which both are very close to the theoretical gravimetric capacity of chloranil (*i.e.*, 220 mA·h/g), become constant and independent of v once the scan rate reaches a sufficiently slow threshold value (dashed vertical lines, depending on the nature and/or pH of the electrolyte), indicating that all quinone molecules in the composite electrode are reversibly reduced for slower scan rates. Interestingly, the threshold scan rate (or time) at which Q_{red} and Q_{ox} change from constant and scan-rate independent to decreasing and scan-rate dependent coincides with the transition in Figure 2i (dashed vertical lines), where $i_{p,red}$ and $i_{p,ox}$ change from nonproportional to proportional to $\sqrt{v}$, for both electrolytes. These observations demonstrate that the classical eq. 13,[75] which states that the peak current in CV is proportional to v for a one-electron Nernstian surface-confined process, is here not applicable.

$$i_p = \frac{F^2}{4RT} v S L C^0_{Q,f} \quad (13)$$

(where $C^0_{Q,f}$ is the starting concentration of the quinone in the electrode composite, S is the geometric electrode area, and L is the thickness of the composite layer). The first reason that invalidates the use of this equation is that the latter is established for a surface electrochemical reaction involving a fast one-electron transfer (Nernstian behavior), whereas here we are dealing with an electrochemical process that involves two electron transfer[76] also coupled with protonations. The second reason is that the electrochemical reaction involves a phase transition with nucleation and growth that is kinetically highly nonlinear. This explains why, at slow scan rates, although the quinone is quantitatively transformed (surface process), the shape of the voltammograms continues to vary, with an increasingly pronounced peak as v decreases (see Figure S1, where slow CVs are normalized to v). These results demonstrate the

need for caution in interpreting peak currents as a function of *v*, echoing what was recently pointed out by C. Costentin[77] and others.[78]

From the slopes of 0.5 in Figure 2i, one can tentatively extract an apparent diffusion coefficient, D_{app}, from the fit of the Randles–Ševčík equation[79] (eq. 14) to the data (keeping in mind that this equation is only valid for an ideal Nernstian redox couple diffusing freely and homogeneously in one compartment, so the D_{app} value extracted with this equation is only a rough estimate).

$$i_p = 2 \times 0.446 F S C^0_{Q,f} \sqrt{D_{app} F v / RT} \quad (14)$$

From the best fits, an average D_{app} value of 4.5×10^{-6} cm^2/s was recovered from the reduction and oxidation peak currents in the acetate buffer, while a D_{app} value of 7.5×10^{-6} and 15×10^{-6} cm^2/s was determined from, respectively, the reduction and oxidation peak currents in the HCl electrolyte. These values are 2 to 12 fold lower than the diffusion coefficients of acetic acid/acetate (1.2×10^{-5} cm^2/s for both molecules[80]) and H_3O^+/H_2O (9×10^{-5} cm^2/s for H_3O^+[81] and 2.2×10^{-5} cm^2/s for H_2O[82]) in water, which are the effective proton donor/proton acceptor couples for reversible PCET reduction of chloranil in the acetate buffer and HCl electrolyte, respectively. This thus supports the hypothesis that the rate-determining process controlling the magnitude of the peak currents is the diffusion of the soluble proton donors/proton acceptors throughout the electrode porosity. That D_{app} values are lower than those in the bulk electrolyte is consistent with the fact that the mass transport inside the porous electrode is reduced by tortuosity and constriction effects.[83-86] However, it is also important to recall that diffusion in porous electrode materials is an inherently complex process, involving subtle interplays between many factors that include not only the size and shape distribution of pores, the tortuosity of diffusion pathways, but also the nature of the electrolyte, its interaction with the solid-liquid interface, and the solvent swelling of active material.[87] Among the mass

transport rate limitations, the diffusion of the buffer components inside but also outside the electrode porosity is certainly the most obvious. As already discussed, it is expected to lead to a local pH gradient for the reason that, in the solid state, the electrochemical reduction/reoxidation of the rather highly concentrated quinone requires a considerable supply of proton donors/acceptors at the electrode interface. If mass transport is not sufficiently rapid, the buffer in the void volume of the pores can no longer maintain the local pH constant, which translates in CV into peak currents proportional to $\sqrt{v}$ and ΔE_p increase (see above). Another possible mass transport rate limitation is through the solid-state diffusion of protons and electrons taking place by proton-coupled electron self-exchanges between the different neighboring solid quinone forms throughout the nonconductive solid active material (*i.e.* the fraction of solid quinones not in contact with either the conductive carbon additive or the inner electrolyte). At a high buffer concentration and relatively slow scan rates, one might therefore expect the limiting diffusional process to: (*i*) the buffer diffusion in the pores, (*ii*) the electrons/protons migration across the solid active material, or (*iii*) a mix of both, ultimately leading to the same dependence of the faradic peak currents on $\sqrt{v}$.[88] Last but not least, the Ohmic drop has also to be taken into account, especially when the scan rate becomes increasingly high.[89] Its contribution was therefore evaluated from Ohmic drop compensation experiments (see Figure S3) and the results show that it remains negligible as long as *v* is below a few mV/s.

The above interpretations inferred from CVs were confirmed from the galvanostatic discharge/charge (GDC) profiles recorded for chloranil and duroquinone electrodes in buffered electrolytes (Figure 3). As shown from the average discharge/charge potential plateaus (or $E_{1/2}$, assumed to be close to E^0_{app}) extracted from the GDC profiles, the values are clearly pH-dependent for both quinones, showing a potential shift of -59 mV/pH over the

entire pH range for duroquinone (Figure 3d), and extending down to pH < 7 for chloranil (Figure 3b). Their comparison with the E^0_{app}-pH diagrams of the same quinones in homogeneous solution shows that they are relatively close, differing mainly by a slight shift to negative potentials (by *ca.* -100 and -50 mV for chloranil and duroquinone, respectively). This potential shift suggests that the reduced forms of chloranil and duroquinone are somewhat destabilized in the solid phase, a result which suggests that the thermodynamic parameters of the PCET mechanisms are slightly altered in the composite electrode environment, but not to the extent of modifying the mechanism or its pathways. That the PCET mechanisms remain almost the same is also supported by the double discharge plateau observed for chloranil at basic pHs (*i.e.*, pHs > 7) (Figure 3b), a behavior that is reminiscent of the two sequential one-electron reductions of chloranil at these pHs (corresponding thus to the process described by reactions 2 and 3 with charge compensation by cations). In an attempt to make a rough assessment of the thermodynamic properties of chloranil within the composite electrode, we have adjusted the values of the four key parameters (*i.e.*, p$K_{a,3}$, p$K_{a,6}$, E_1^0 and E_2^0) in such a way to fit eqs. 5, 6 and 9 as close as possible to the experimental data (see the solid curves in Figure 3b). From the best fit, the following values were then recovered: p$K_{a,3}$ = 9.0, p$K_{a,6}$ = 7.0, E_1^0 = -0.014 V and E_2^0 = -0.115 V. Their comparison with the values previously extracted from the electrochemistry of chloranil in solution (p$K_{a,3}$ = 8.5, p$K_{a,6}$ = 5.8, E_1^0 = 0.12 V and E_2^0 = -0.03 V) allows concluding that the composite matrix has the effect to slightly increase the apparent pK_as of reduced chloranil and to somewhat decrease the formal potentials of $Q/Q^{\bullet-}$ and $Q^{\bullet-}/Q^{2-}$ (by a value of -135 mV and -75 mV, respectively). This relatively weak influence of the electrode material environment suggests that the aqueous electrolyte and its constituents (notably the weak acid and conjugate base of the buffer) have a good access to the entire inner surface area of the porous electrode, and that, ultimately, quinone molecules find themselves in an environment that is not so different from the

aqueous electrolyte. This probably explains why, regardless of pH and nature of the buffered electrolyte, the discharge capacities recovered with chloranil electrodes are optimal (*i.e.*, ranging from ~200 to 250 mA·h/g, with an average value centered on 225 ± 5 mA·h/g) and close to the expected theoretical value (*i.e.*, 220 mA·h/g). This full exploitation of the redox-activity of chloranil is however not transposable to

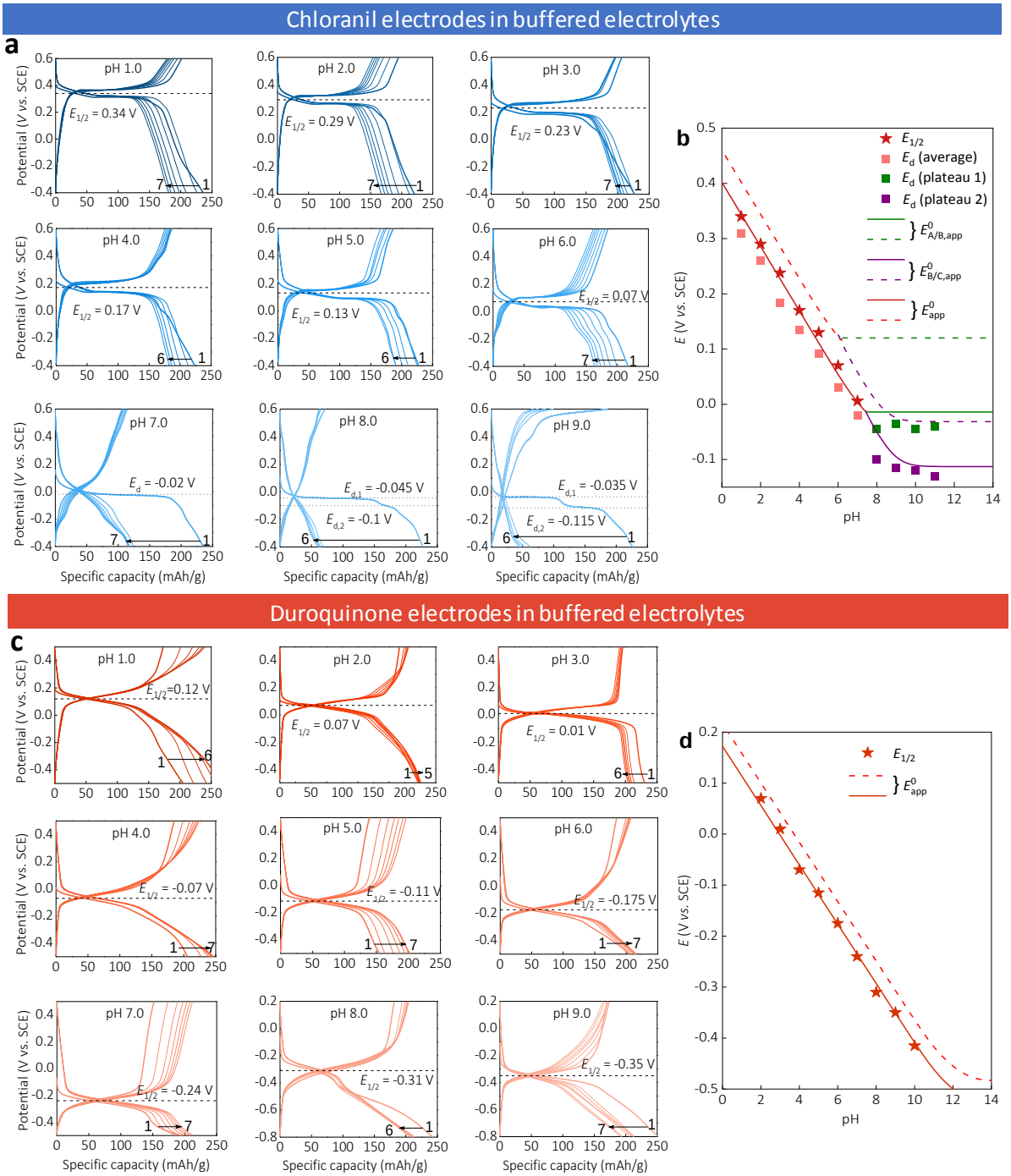

Figure 3. (a) GDC cycling profiles (the first 5 to 7 cycles are shown and the first cycle is highlighted in bold) of Ketjenblack EC-300J carbon-based chloranil electrodes (rate: 0.5 mA/cm^2) in a set of buffered electrolytes at different pHs (the pH values are indicated on the graphs). (b) Average discharge potentials (E_d) of the single (red solid squares) or two plateaus (green and purple solid squares) extracted from the first galvanostatic discharges as a function of pH. The red solid stars correspond to the $E_{1/2}$ extracted from the GDC cycles as a function of pH. The dashed red, green and purple curves are the theoretical E-pH plot of chloranil in homogeneous solution (same plots than in Figure 1c), while the solid green, purple and red curves are the best fits of eqs. 5, 6 and 9, respectively, to the experimental data using: p$K_{a,3}$ = 9.0, p$K_{a,6}$ = 7.0, E_1^0 = -0.014 V and E_2^0 = -0.115 V. (c) GDC cycling profiles (the first 5 to 7 cycles are shown and the first cycle is highlighted in bold) of Ketjenblack EC-300J carbon-based duroquinone electrodes (rate: 0.5 mA/cm^2) in a set of buffered electrolytes at different pHs (the pH values are indicated on the graphs). (d) (red stars) Average discharge/charge plateau potential (or $E_{1/2}$) extracted from the GDC cycles in c as a function of pH. The dashed red curve is the theoretical E^0_{app}-pH plot of duroquinone in homogeneous solution (same plot than in Figure 1g), and the solid red line is the same as the dashed red line but vertically offset by -50 mV.

duroquinone, which on average delivers only two-thirds of the theoretical gravimetric capacity (*i.e.*, ~215 ± 30 mA·h/g over the theoretical value of 330 mA·h/g). To better understand the reason for this low utilization of duroquinone, we hypothesized that it could result from a fraction of quinones in the composite matrix that has limited or no access to either the carbon conductor for electron exchange or the electrolyte for proton or cation exchange. This assumption is supported by the fact that capacities were observed highly dependent on the type of carbon-based powder used for the slurry preparation. Indeed, during our preliminary experiments conducted with Super P® as carbon black the gravimetric capacities were found consistently lower than those obtained with the carbon powder Ketjenblack EC-300J (on average ~150 mA·h/g, which corresponds to ~68% and ~45% of the theoretical capacity of chloranil and duroquinone, respectively – see Figures S4 and S5). We have attributed this effect to the higher specific surface area of Ketjenblack EC-300J (800 m^2/g) as compared with Super P® (60 m^2/g), the former being expected to promote/maximize the electrical connection between the 3D network of conductive carbon nanoparticles and the nonconductive redox-active organic molecules, as well as the access to the electrolyte. This critical role played by the carbon conductor was further confirmed with the Ketjenblack EC-600JD, whose specific surface area is higher (1400 m^2/g). Indeed, thanks to the use of this ultraporous carbon conductor, we succeeded in preparing duroquinone electrodes with the expected maximal gravimetric capacity (> 300 mA·h/g, see Figure S6).

Another important piece of information revealed by the GDC cycling experiments is the severe loss of chloranil electrode's capacity as soon as the pH exceeds 6.0 (Figure 3a), whereas such an effect is inexistent with the duroquinone electrodes (Figure 3c). A full capacity loss is even observed from the very first discharge at pHs > 8.0, and it is accompanied by an equally rapid yellowing of the aqueous electrolyte (see Figure S7), signing the dissolution of the reduced forms of chloranil. That the reduced quinone is highly

soluble at pHs > 7 is not a surprise since the predominant reduced forms at these pHs are the negatively charged QH^- and Q^{2-} species (see *E*-pH diagram in Figure 1c), which *a priori* are much more hydrosoluble than the neutral protonated QH_2 species. A solubility test was thus carried out with the commercially available reduced form of chloranil, *i.e.* the tetrachloro-1,4-hydroquinone. The image of the flasks in Figure S8 demonstrates that the tetrachloro-1,4-hydroquinone is effectively highly soluble in a borate buffer of pH 7, while not at all in an acetate buffer of pH 5. The fact that the reduced duroquinone does not lead to an analogous strong capacity loss can be easily understood from its pK_a values of 11.2 and 12.9, which are both definitely too high for leading to the formation of the water-soluble reduced species QH^- and Q^{2-}, even at the highest pHs explored here.

2.3 Electrochemistry of chloranil and duroquinone in unbuffered aqueous electrolytes

Since aqueous electrolytes for zinc-organic batteries are commonly prepared by dissolving a Zn^{2+} salt in water, they are not buffered. Consequently, the quinone PCET mechanisms validated above for aqueous buffers can potentially be different in unbuffered electrolytes. It is therefore important to understand the consequences of unbuffered conditions on the electrochemical behavior of chloranil and duroquinone. To this end, we repeated the CV experiments on dilute quinone solutions, but this time in different unbuffered aqueous electrolytes prepared with different mono and divalent salts, *i.e.* KCl, NaCl, LiCl, $MnCl_2$, $ZnCl_2$, $AlCl_3$, and $Pb(NO_3)_2$. The interest of these salts is that their dissolution in water leads to the formation of dissociated metal cations that are more or less strongly coordinated (or solvated) by several molecules of water. Depending on the size and electronic charge density of the metal cation, the Brønsted acidity of these coordinated water molecules can be much higher than that of normal water. In the case of multivalent cations, most are known to lead in

the formation of metal hexaaqua complexes, the weak acidity of which is governed by the following acid-base equilibrium in water (or protolysis reaction):

$$\left[M(H_2O)_6 \right]^{n+} + H_2O \overset{K_a}{\rightleftharpoons} \left[M(H_2O)_5(OH) \right]^{(n-1)+} + H_3O^+ \qquad (15)$$

where M is a metal ion and n = 2 or 3. This equilibrium is thus characterized by a pK_a value which varies with the nature of the metal ion. As a result, these solvated weak acidic metal aquo ions can thus play the role of proton donor during the reversible reduction of quinone. This is analogous to what we previously revealed for the charge storage mechanisms of TiO_2, WO_3 and MnO_2 in mild Al^{3+}- and Zn^{2+}-based aqueous electrolytes, and where we demonstrated that the metal aquo-complexes $\left[Al(H_2O)_6 \right]^{3+}$ and $\left[Zn(H_2O)_6 \right]^{2+}$ present in the electrolyte are responsible for the reversible insertion of protons in TiO_2 and WO_3,[90, 91] or, alternatively, of the reversible proton-coupled electrodissolution of MnO_2.[92-94] This is also what prompted, very recently, Poizot's group to show that $\left[Zn(H_2O)_6 \right]^{2+}$ ions in a mild aqueous electrolyte contribute to the reversible protonation of a 2,5-ditertbutyl hydroquinone-based organic electrode, thereby challenging the prevailing assertion of reversible Zn^{2+} insertion in zinc-organic batteries.[95]

According to the literature, the pK_a values for the selected metal aquo cations at 25°C are in order of increasing acidity: $K^+ > Na^+ > Li^+ > Ca^{2+} > Mg^{2+} > Mn^{2+} > Zn^{2+} > Pb^{2+} > Al^{3+}$.[96] Since the dissolution of these metal cations in water modifies more or less the acidity of the resulting aqueous solutions, the pHs of these metal salt solutions (at 0.5 M) were measured (see Table 1).

The CVs of chloranil and duroquinone recorded in the unbuffered monovalent cation electrolytes (*i.e.*, 0.5 M KCl, NaCl or LiCl) show that they all overlap (Figure 4a and 4e), indicating that the nature of the monovalent cation has no influence on the electrochemistry of

Table 1. pK_a of different metal aquo cations used in this work and pH of the corresponding 0.5 M metal salt aqueous solutions.

Metal salt	KCl	NaCl	LiCl	$CaCl_2$	$MgCl_2$	$MnCl_2$	$ZnCl_2$	$Pb(NO_3)_2$	$AlCl_3$
pK_a of $[M(H_2O)_x]^{n+}$ [96]	14	13.9	13.6	12.7	11.2	10.6	9.0	7.6	5.0
pH*	6.4	6.2	6.2	6.1	5.6	5.3	5.0	3.5	2.5

* determined with an uncertainty of ± 0.2 pH unit

the quinones. Additionally, for chloranil, the CVs systematically exhibit two reversible waves, whose potential positions (0.1 and -0.1 V) are close to the values characterizing the two sequential one-electron reductions of chloranil without protonation. This behavior is due to the absence of a sufficiently acidic proton donor in the electrolyte (the pK_as of the hydrated monovalent ions are close to the pK_a of water and too weak to contribute to the protonation of $Q^{\bullet-}$ or Q^{2-}), so the electrochemical reduction of chloranil follows the two sequential one-electron reductions path (*i.e.*, the upper horizontal pathway of the square scheme mechanism in Scheme 2). This also implies that during the forward reduction, the local pH at the electrode/electrolyte interface is significantly increased (*vide infra*).

On the other hand, CVs of chloranil and duroquinone recorded in the multivalent cation electrolytes show reversible waves that steadily increase towards positive potentials as the Brønsted acidity of the hexaaqua metal cation increases (Figure 4a and 4e). In the case of chloranil, the CVs even switch from two waves of 1 e^- to one wave of 2 e^-, which is characteristic of the PCET square scheme mechanism described above in buffered electrolytes. These behaviors indicate that the metal aquo cations are directly involved in the PCET reduction of quinones (by direct involvement, we mean that it is the metal aquo cations that participate as proton donors in the electrochemical reaction and not the free protons, *i.e.* H_3O^+, in solution, a statement which remains valid regardless of whether the proton-electron transfer is sequential

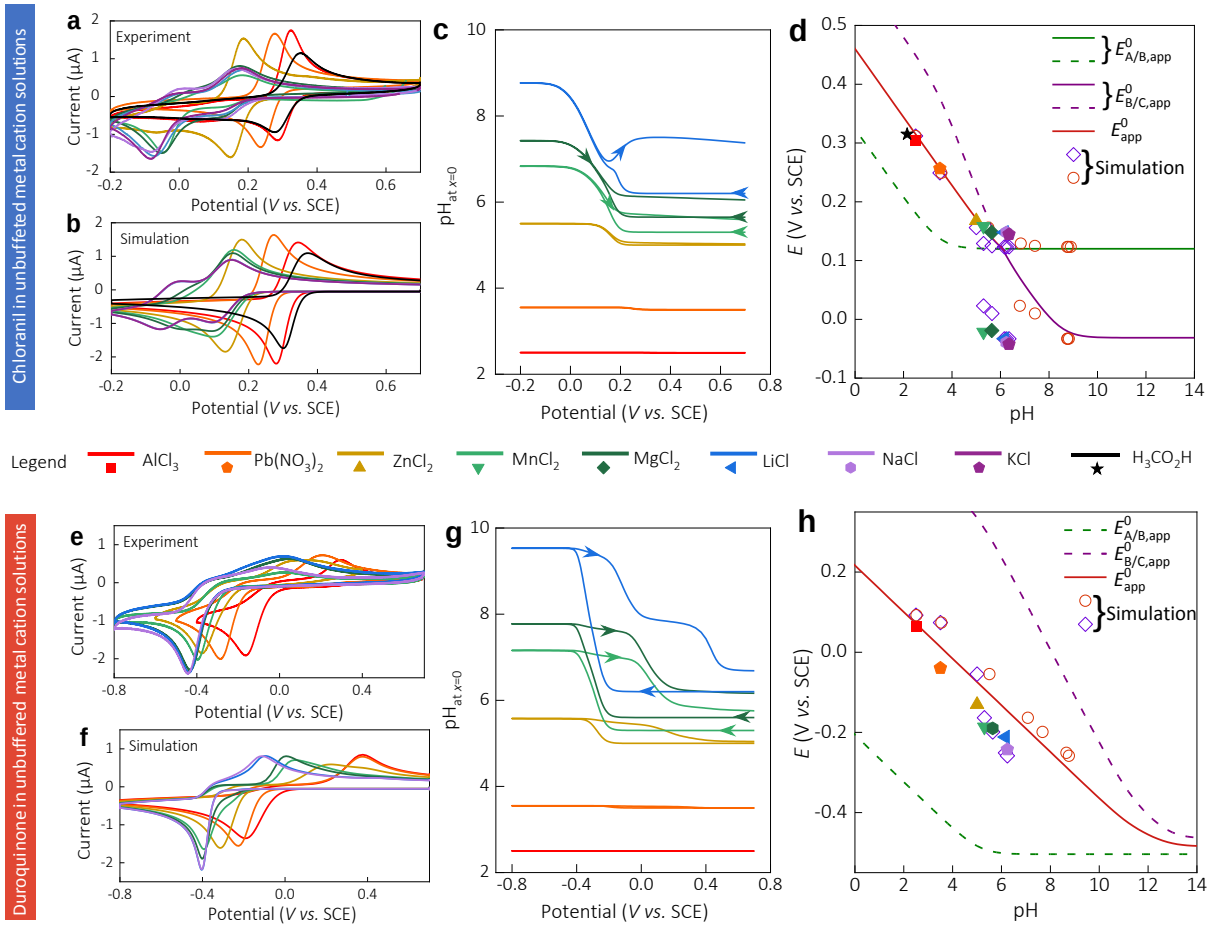

Figure 4. CVs of 0.1 mM (a, b) chloranil or (e, f) duroquinone in unbuffered electrolytes (0.5 M) prepared from different salts (the code color for the nature of the salt is indicated in the graph legend). Scan rate: 30 mV s^{-1}. The experimental (a, e) and simulated (b, f) results are plotted separately. (c, g) Simulated local pH changes (*i.e.*, at the electrode surface x = 0) as a function of potential (extracted from CV simulations). (d, h) E-pH diagrams of (d) chloranil and (h) duroquinone, where colored solid symbols are $E_{1/2}$ extracted from the experimental CVs (*i.e.*, average of $E_{p,c}$ and $E_{p,a}$) and plotted as a function of bulk pH, while empty dot and empty diamond symbols are $E_{1/2}$ extracted from the simulated CVs and plotted, respectively, as a function of the experimental bulk pH and simulated local pH (*i.e.*, the average $pH_{x=0}$ simulated at the end of the forward reduction scan). The solid and dashed green, purple and red curves are the same theoretical plots than those in Figures 1c and 1g.

or concerted[51]). It's also important not to confuse the protons involved as charge carriers (*i.e.*, in the solid state) with the source of protons in the electrolyte. For each unbuffered solutions, if we report $E_{1/2}$ as a function of bulk pH (Figures 4d and 4h) we observe for the most acidic divalent cations a rather good correlation with a dependence of -59 mV per pH unit (the data align parallel to the -59 mV/pH slope of the theoretical plot of E^{0}_{app}). This further confirms that protons are involved in the quinone reduction process and that they stem from the weak acid metal aquo cations present in the electrolyte, as follows:

$$Q + 2\left[M\left(H_2O\right)_x\right]^{n+} + 2\,e^- \rightleftharpoons QH_2 + 2\left[M\left(H_2O\right)_{x-1}OH\right]^{(n-1)+} \quad (16)$$

An additional experiment, demonstrating that hydrated metal cations perform a role analogous to that of a weak organic acid, is the CV of chloranil we have recorded in an unbuffered solution of acetic acid (0.5 M, pH 2.15) (black curve in Figure 4a). As the pK_a of acetic acid (4.76) is very close to that of $[Al(H_2O)_6]^{3+}$ (5.0), one would expect the CV recorded in each electrolyte to almost overlap. This is indeed what we observe in Figure 4a, where the CVs in acetic acid and Al^{3+}-based electrolytes (compare red and black curves) show an almost overlay of the 2 e^- reversible waves (leading to virtually identical $E_{1/2}$ in Figure 4d).

It is noted that the global electrochemical reaction 16 remains effective if the pK_a of the metal aquo complex remains sufficiently acidic relative to the pK_as of QH_2, since otherwise the electrochemical reaction will have the tendency to follow the upper horizontal pathway of the square scheme mechanism, as shown above for chloranil. On the contrary, in the case where the pK_as of QH_2 are very high such as for the hydroduroquinone, the solvent water is acidic enough to play the role of a proton donor during the reversible proton-coupled reduction of quinone as follows:

$$Q + 2\,H_2O + 2\,e^- \rightleftharpoons QH_2 + 2\,OH^- \quad (17)$$

For the CVs in Figures 4a and 4e, the development of a local pH gradient at the electrode interface should therefore translate into a potential shift of the reversible wave, the greater the local pH change during the CV scan. This is what we observe for the less acidic metal aquo cations, which lead to a negative $E_{1/2}$ shift relative to the equilibrium potentials of the Pourbaix diagrams (Figures 4d and 4h).

To confirm that pH gradients are generated under these experimental conditions and to determine their amplitude, the square mechanisms in CVs were numerically simulated under

unbuffered conditions. For the sake of simplicity, these simulations take into account the metal aquo ion concentration, considering only its first pK_a value and the initial pH of the electrolyte (see the SI for details). The simulated CVs (gathered in Figures 4b and 4f for, respectively, chloranil and duroquinone) finally reproduce quite well the experimental CVs (Figures 4a and 4e). The $E_{1/2}$ extracted from the simulated CVs also agree with the experimental ones in Figures 4d and 4h (this is particularly true for chloranil, but a little less so for duroquinone, at least for the $E_{1/2}$ recovered for Pb^{2+} and Zn^{2+} electrolytes which turn out to be somewhat more positive than the experiment[97]). From the digital CV simulations, the local pH change (*i.e.*, at the electrode surface $x = 0$) extracted as a function of potential (see Figures 4c and 4g) shows that it becomes all the more significant as the acidity of the metal aquo cation becomes lower, thus agreeing with our above expectations. By replotting the $E_{1/2}$ values extracted from the simulated CVs as a function of the simulated local pH (*i.e.*, the average local pH simulated at the end of the forward reduction scan), we obtain a better match with the equilibrium potentials of the Pourbaix diagram (red empty dot symbols in Figures 4d and 4h). Finally, all of these good agreements between simulations and experiments demonstrate the validity of our reasoning and interpretations.

2.4 Electrochemistry of chloranil and duroquinone composite electrodes in unbuffered aqueous electrolytes

With this knowledge in mind, the next step was to examine the galvanostatic discharge/charge profiles (GDC) of chloranil- and duroquinone-electrodes in the unbuffered electrolytes of metal ion salts (Figures 5 and 6, respectively). For the most acidic metal aquo cations (*i.e.* $[Al(H_2O)_6]^{3+}$, $[Pb(H_2O)_6]^{2+}$, $[Zn(H_2O)_6]^{2+}$ and $[Mn(H_2O)_6]^{2+}$) the GDC profiles indicate a fairly reversible charge storage process that reaches gravimetric capacities similar to those previously achieved in buffered electrolytes. Moreover, although the capacity fading is

slightly more pronounced for the Zn^{2+}- and Mn^{2+}-based electrolytes, all globally remain reasonable and comparable to that previously observed in buffered media. In contrast, for the less acidic metal aquo cations (*i.e.*, Ca^{2+} and K^{+}) an almost complete capacity loss is observed for chloranil after just one cycle, while a very high voltage hysteresis between charge and discharge is obtained for duroquinone. These results are in agreement with the above demonstration that the PCET mechanism of quinones persists in the composite electrodes and that metal aquo complexes in the electrolyte are the source of protons when the latter are sufficiently acidic to protonate the reduced forms of quinones. Indeed, the strong capacity fading of the chloranil electrode when working in a $CaCl_2$ or KCl electrolyte is the concrete illustration that in the absence of a sufficiently acidic proton donor in solution, the reduced anionic forms of chloranil cannot protonate, leading to their fast dissolution (similar to what we have seen above in basic buffers). In contrast, in the presence of sufficiently acidic metal hexaaqua ions, the reduced forms of chloranil can protonate, avoiding their dissolution and so authorizing their cycling.

Another element of information which confirms that, with the most acidic metal aquo cations, we are dealing, for both quinones, with a storage mechanism involving reversible charge compensation by protons is that the average discharge/charge potentials (or $E_{1/2}$) extracted from Figures 5 and 6 align almost linearly with a slope of -59 mV/pH when plotted against the bulk pH of unbuffered electrolytes (see Figures 5k and 6k). That a PCET mechanism is at work can also be drawn from the huge voltage hysteresis observed with duroquinone. This behavior is analogous to the one we recently reported for the insertion of protons in TiO_2.[98] This hysteresis is caused by the strong pH gradients which develop at the interface of the composite electrode, especially when the proton donors in the electrolyte become very weakly acidic, as is the case with Ca^{2+}- and K^{+}-based electrolytes. Given the low pK_a values of these two metal aquo cations (12.7 and 13.9, respectively), close to water, it can be considered that

water itself plays the role of proton donor during the electrochemical reduction of duroquinone, leading as per eq. 17 to the release of the strong OH^- base at the electrode interface. In the KCl electrolyte, the local

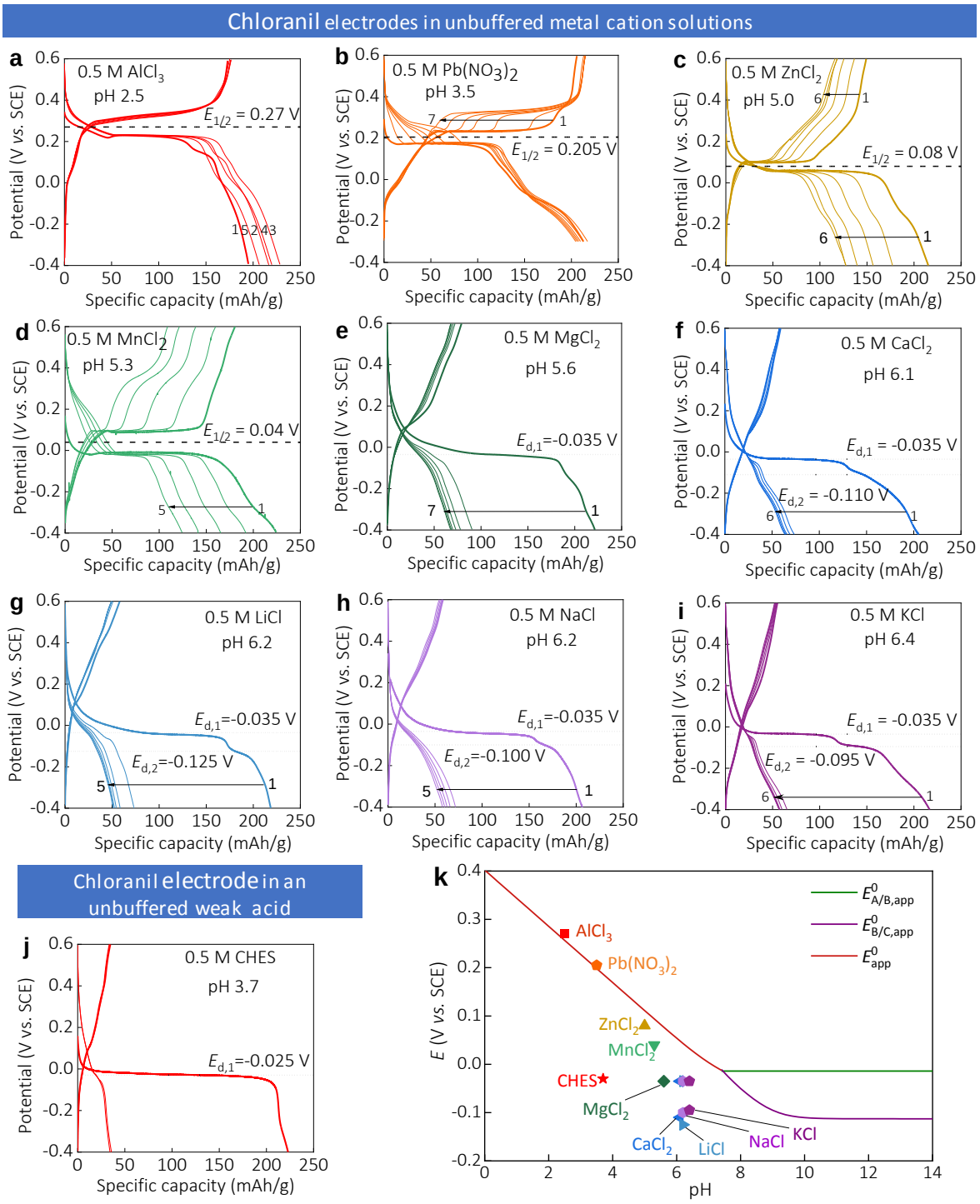

Figure 5. (a-j) Continuous GDC profiles (5 to 7 cycles are shown and the first cycle is highlighted in bold) of Ketjenblack EC-300J carbon-based chloranil electrodes (rate: 0.5 mA/cm^2) in 0.5 M unbuffered electrolytes prepared from different salts (the nature of salt and bulk pH of the solution are as indicated on the graphs). The dashed horizontal lines represent the $E_{1/2}$, while the dotted horizontal lines are the average discharge plateau potential, E_d. (k) E-pH plots obtained from the $E_{1/2}$ values

(*i.e.*, average of discharge and charge plateau potentials) and $E_{d,1}$ and $E_{d,2}$ (*i.e.*, discharge potentials of the first and second plateaus) extracted from the GDC profiles in graphs a to j. Solid red, green and purple lines are the same theoretical plots than in Figure 3b.

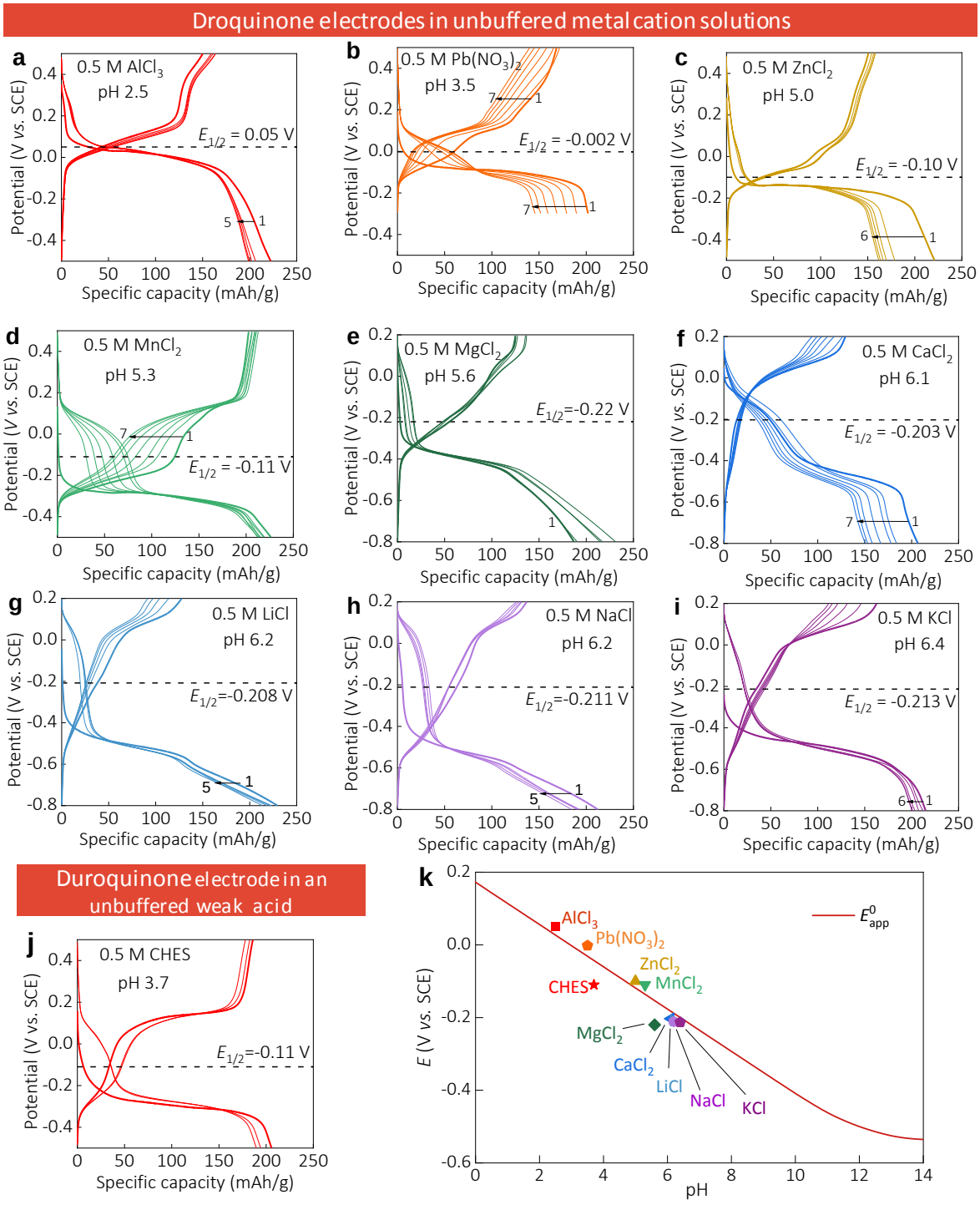

Figure 6. (a-j) Continuous GDC profiles (5 to 7 cycles are shown and the first cycle is highlighted in bold) of Ketjenblack EC-300J carbon-based duroquinone electrodes (rate: 0.5 mA/cm^2) in 0.5 M unbuffered electrolytes prepared from different salts (the nature of salt and bulk pH of the solution are as indicated on the graphs). The dashed horizontal lines represent the $E_{1/2}$. (k) *E*-pH plots obtained from the $E_{1/2}$ values (*i.e.*, average of discharge and charge plateau potentials) extracted from the GDC profiles in graphs a to j. The solid red line is the same theoretical plot than in Figure 3d.

rise in pH cannot lead to KOH precipitation as the latter is highly soluble in water, whereas with $CaCl_2$, the solubility product of $Ca(OH)_2$ remains relatively high (*i.e.*, K_s = 6.4 ×10^{-6} mol^3/L^3 at 25°C[99]), so its precipitation is also unlikely (it can only start when pH is > 12[99]).

Under these conditions, the duroquinone electrode, with its high solid-state concentration, can be viewed as a proton sponge which, during discharge, locally generates a high concentration of soluble hydroxide ions, which then diffuse from the electrode into the bulk electrolyte. On account of the thermodynamic cost of dissociating a proton from water, a highly negative discharge potential has to be reached to reduce duroquinone into QH_2, thereby explaining why the discharge takes place at such highly negative potentials. During the following galvanostatic recharge, the huge quantity of protons released from reoxidation of the duroquinone electrode rapidly neutralizes the small amount of hydroxide bases still present in the diffusion layer, and next locally and strongly acidifies the unbuffered electrolyte. This leads to an abrupt drop in the local pH and, corollary, to a large rise in the charging potential, until it stabilizes at a high value when the local H_3O^+ concentration becomes sufficiently high and so relatively constant. This finally means that in both the $CaCl_2$ and KCl electrolytes, the discharging reaction does not involve the same proton donor/acceptor couple than the charging reaction, as follows:

Discharge process: $Q + 2\,H_2O + 2\,e^- \rightarrow QH_2 + 2\,OH^-$

Charge process: *at the beginning* $QH_2 + 2\,OH^- \rightarrow Q + 2\,H_2O + 2\,e^-$

on the plateau $QH_2 + 2\,H_2O \rightarrow Q + 2\,H_3O^+ + 2\,e^-$

It is important to recall here that metal aquo complexes possess several Brønsted acidities with close pK_as, which, after several deprotonation steps, can potentially lead to the precipitation of insoluble metal hydroxides.[99] As a result, the following global reversible

electrochemical process, including precipitation/redissolution of metal hydroxides, can occur during the reversible electrochemical reduction of a quinone:

$$Q + \frac{2}{n}\left[M\left(H_2O\right)_x \right]^{n+} + 2\,e^- \rightleftharpoons QH_2 + \frac{2}{n}\left[M\left(H_2O\right)_{x-n}\left(OH\right)_n \right]\downarrow \qquad (18)$$

In such a process, the moment at which the metal hydroxide begins to precipitate depends on the amount of protons locally consumed by the reduced quinone, and therefore on the extent of the local pH increase in the vicinity of the electrode. This local pH increase also depends on the pK_as and concentration of metal aquo cation present in the unbuffered electrolyte, as well as on the solubility product of metal hydroxide. Furthermore, once precipitation starts, the local pH should stabilize and also remain stable during the subsequent QH_2 to Q reoxidation step for the reason that the insoluble metal hydroxide accumulated at the electrode during discharge should facilitate (thermodynamically) the reverse reaction of eq.18.[100] Given the very low solubility products of the various selected metal cations, there is no doubt that, for the most acidic of them (thus excluding $CaCl_2$ and electrolytes based on monovalent cations, as discussed above), a metal hydroxide precipitate is formed during discharge of the quinone-based electrodes.

To better understand the impact that a metal hydroxide precipitate can have on the shape of GDC curves and, in particular, on the voltage hysteresis, the chloranil- and duroquinone-based electrodes were cycled in a 0.5 M N-cyclohexyl-2-aminoethanesulfonic acid (CHES), *i.e.* an unbuffered weak organic acid electrolyte for which the conjugate base cannot precipitate whatever the pH. This zwitterionic weak organic acid has a pK_a of 9.3, close to the pK_a of $[Zn(H_2O)_6]^{2+}$. The pH of a 0.5 M CHES solution is thus mildly acidic, *i.e.* pH 3.7, slightly more than the 0.5 M $ZnCl_2$ solution (pH 5.0). The GDC profiles of the two quinone electrodes in CHES are given in Figure 5j and 6j. Their comparison with the GDC profiles recorded in $ZnCl_2$ (Figure 5c and 6c) shows a contrasting behavior, and despite the similar

pK_a values of CHES and $[Zn(H_2O)_6]^{2+}$. Indeed, for the chloranil electrode in CHES we observe a total loss of capacity from the first cycle, whereas in $ZnCl_2$ the electrode is capable of cycling reversibly (also with a slightly more positive discharge potential than in CHES). For the duroquinone electrode, it reversibly cycles in both electrolytes, but with a higher voltage hysteresis in CHES compared to $ZnCl_2$. These differences are clearly the consequence of the zinc hydroxide precipitation on top of the electrode surface when working in $ZnCl_2$ as opposed to CHES. The formation of zinc hydroxide in $ZnCl_2$ is attested by the more positive value of the discharge potential in $ZnCl_2$ than in CHES. This more positive value is caused by a stop in the local pH increase when zinc hydroxide begins to precipitate. As a consequence, reversible PCET reduction of chloranil is enabled in $ZnCl_2$ (Figure 5c) but not in CHES (Figure 5j), in which the greater local pH increase entails irreversible dissolution of the unprotonated reduced chloranil. A similar behavior is observed for duroquinone, with the difference that the PCET reduction of duroquinone in CHES is chemically reversible due to the absence of dissolution of the protonated reduced form, but with the counterpart of much larger pH swings resulting in huge voltage hysteresis (Figure 6j) compared to $ZnCl_2$ (Figure 6c).

To check whether a metal hydroxide forms during the discharge of chloranil electrodes in unbuffered metal ion electrolytes, the electrode surface was characterized by scanning electron microscopy (SEM) coupled with energy dispersive X-ray spectroscopy (EDX). A comparison of the images of chloranil electrode before and after discharge in a $ZnCl_2$ electrolyte (Figure 7a and 7b, respectively) clearly reveals the presence of small needles of ~100 µm length on the discharged electrode surface, which EDX element mapping shows to be mainly composed of Zn and O, thus consistent with a zinc hydroxide precipitate. The formation of a metal hydroxide can also be seen on the image of the chloranil electrode discharged in $Pb(NO_3)_2$ electrolyte (Figure 7c), forming onto the surface a carpet of small

ribbon-like strands (around 10 µm long) whose composition clearly indicates the presence of Pb and O. The image also reveals the presence of thicker, sparse rods, approximately 3 to 5 µm in diameter and 100 µm long, whose elemental mapping indicate they are composed of C, O and Cl, but not of Pb. These rods are therefore likely to correspond to the tetrachloroquinone in its reduced form. The same rods of reduced chloranil are also observed on the image of the chloranil electrode discharged in $AlCl_3$,

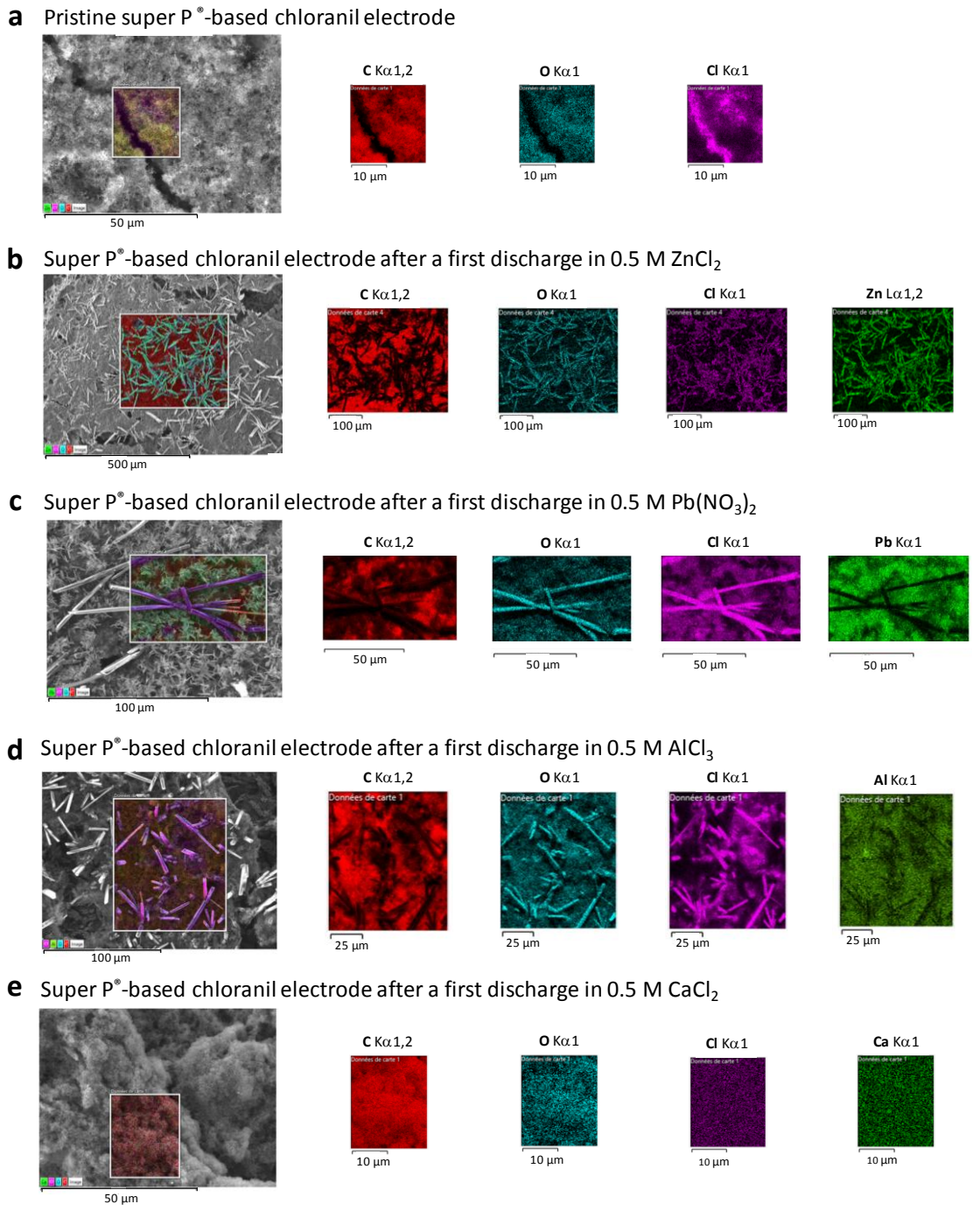

Figure 7. SEM images and EDX mapping (the mapped elements are indicated on top of the images) of the surface of Super P® carbon-based chloranil electrodes (a) before and (b-e) after a single discharge in the following unbuffered electrolytes: (b) 0.5 M $ZnCl_2$, (c) 0.5 M $Pb(NO_3)_2$, (d) 0.5 M $AlCl_3$, and (e) 0.5 M $CaCl_2$.

but without any evidence of a metal hydroxide precipitate (the absence of aluminum hydroxide does not mean that it does not form. It is indeed plausible that the precipitate rapidly redissolves as soon as the electrode is disconnected, then removed from the electrolyte and rinsed with Milli-Q water). Interestingly, no rods or precipitates form at the chloranil electrode discharged in $CaCl_2$, consistent with the fact that the reduced Q^{2-} form of chloranil, under these conditions, no longer protonates and therefore dissolves in the electrolyte (same results were obtained in KCl – not shown). These experiments were replicated with the Ketjenblack carbon-based chloranil electrodes and they were shown to produce almost similar results (Figure S9), with SEM images showing the systematic presence of these sparse, 100-µm-long rods of reduced chloranil on the electrode surface when discharged in a sufficiently acidic metal aquo cation-based electrolyte. These results are thus a further confirmation that in these electrolytes the reduced Q^{2-} species protonates into QH_2, which given its insolubility at pH < 7 (Figure S8) remains trapped within the porosity of the composite matrix. It is also possible that, given the pH gradients that are expected to develop within the electrode porosity, a small fraction of the Q^{2-} species has time to escape the electrode porosity and then protonate definitively at the electrode/solution interface, forming these insoluble QH_2 rods by nucleation and growth.

To further confirm that chloranil in the composite matrix of the electrode is effectively reduced into its QH_2 form, the composite electrodes were characterized by standard X-ray diffraction spectroscopy (XRD) before and after their single discharge in both $AlCl_3$ and $ZnCl_2$. The resulting XRD patterns in Figure S10 show that the characteristic peaks of chloranil are, after discharge in $AlCl_3$ and $ZnCl_2$ electrolytes, converted to peaks corresponding to the tetrachloro-1,4-hydroquinone. For the chloranil electrode in $ZnCl_2$, the additional presence of peaks correlates with *a priori* a zinc hydroxide phase that we do not observe with the chloranil electrode discharged in $AlCl_3$. These observations are in good

agreement with the conclusions drawn from the SEM images and EDX mappings, namely the absence of an aluminum hydroxide precipitate after discharge in an $AlCl_3$ electrolyte, in contrast to the formation of a zinc hydroxide precipitate on the electrode surface after a first discharge in a $ZnCl_2$ electrolyte.

2.5 GDC simulations

In order to definitely confirm the validity of the different mechanistic interpretations inferred from the shape of the galvanostatic curves recorded under different experimental conditions, we have carried out their numerical simulation on the basis of a two-compartment 1D transport-reaction model (see Scheme S1 in SI). Starting from the current collector, the first compartment was used to model the finite porous film electrode of thickness L (100 µm) containing the quinone and the electrolyte components, while the second compartment, adjacent to the first, was used to model the semi-infinite electrolyte with its different constituents. The two compartments were separated by the film/electrolyte interface through which the electrolyte components can reversibly cross according to an equilibrium partitioning governed by k_{on} and k_{off} rate constants. To take into account the possible dissolution of the reduced forms QH^- and Q^{2-} into the electrolyte, a dissolution rate constant $k_{dis,off}$ was considered for these two species. To avoid the complexity of modeling charges and electrons transport throughout the porous composite electrode matrix, we have considered that the quinone-based redox-active species are homogeneously distributed in the first compartment and able to rapidly freely diffuse in order to exchange electrons at the current collector/film boundary (see Scheme S1 in SI). By selecting, for all the different quinone forms in the film, an artificially fast film diffusion coefficient (*i.e.*, 10^{-4} cm^2/s), this amounts (under reasonable charge/discharge rate conditions) to an electrochemical process where the redox-active species are almost instantaneously reduced or oxidized irrespective of their position within the film, thus resulting in the absence of concentration gradients across the

film. Regarding the diffusion coefficients of the electrolyte components within the film compartment, they were assumed to be one-third to one-tenth slower than those in the electrolyte. As for the CV simulations in a homogeneous solution, the square-scheme mechanism with its thermodynamic parameters was settled to the film compartment. In addition, the standard Butler-Volmer formalism was applied to all elementary electrochemical reactions (with α values of 0.5), also assuming that the heterogeneous ET rate constants are the same as in solution.

A selection of GDC profiles simulated for different pH conditions as well as for buffered and unbuffered electrolytes are plotted in Figure 8 (middle graphs) and compared with those obtained experimentally (left graphs) for each quinone. Although the modeling is approximate, the simulated GDC profiles reproduce quite well the experimental data, particularly the potential positioning of the GDC plots, which varies with pH, but also the reversible or irreversible behavior of the galvanostatic cycle as a function of pH and nature of the quinone, as well as the pronounced potential hysteresis that arises when the duroquinone-based electrode is cycled in the unbuffered CHES electrolyte. From simulations, we were also able to plot the local variation in pH upon cycling (right graphs in Figure 8), and the resulting plots illustrate quite clearly the sharp pH gradients which develop at the electrode interface when cycled in unbuffered electrolytes (Figures 8f and 8l).

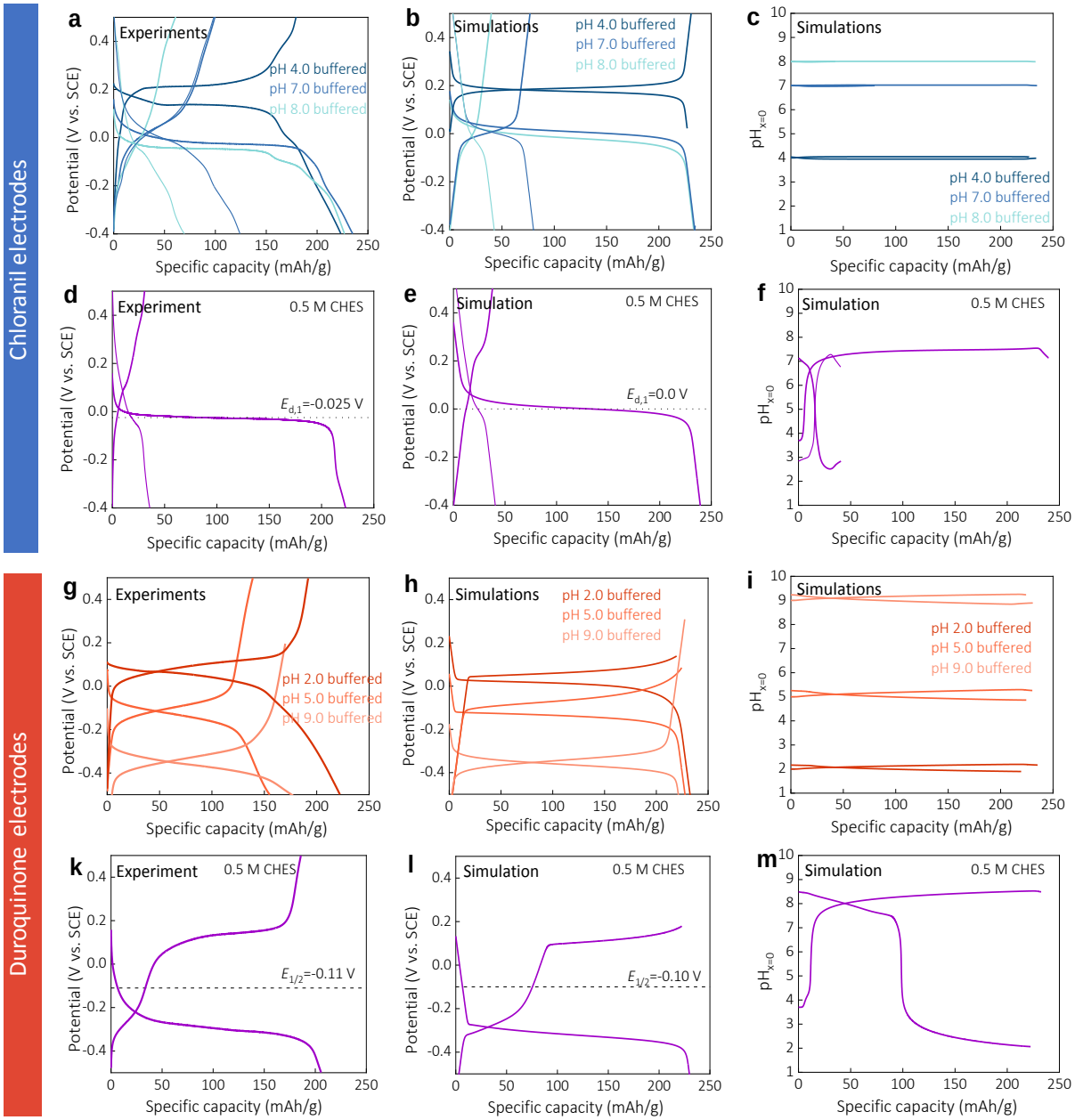

Figure 8. GDC cycles recovered (left) from experiments compared with those obtained (middle) from numerical simulations (see text and SI for details) at different pHs and either under buffered or unbuffered conditions (see legend on the graphs). The right graphs are to the local pH evolution (*i.e.*, at x = 0) extracted from simulated galvanostatic cycles. The top graphs from a to f are for the chloranil-based electrode, while the bottom graphs from g to l are for the duroquinone-based electrode.

3 Conclusions

In this work, we demonstrate that the PCET square scheme mechanism, well-established for quinones in aqueous electrolytes, remains valid for quinones incorporated within the solid matrix of organic electrodes. We also show that pK_as of the reduced forms of quinone in the composite electrode are key elements that determine whether the charge-compensating cation

(or charge carrier) is the proton supplied by the proton donor in the electrolyte or, alternatively, the cation present in the electrolyte. In the case of duroquinone, whose QH_2 pK_as are very basic (> 11), the discharge/charge storage mechanism is exclusively based on proton uptake/release whatever the pH. On the contrary, in the case of chloranil whose QH_2 pK_as are much more acidic (7.0 and 9.0), the proton uptake/release is only effective at pH values below 7.0, since at higher pHs, the cation in the electrolyte takes over to compensate for the negative charges of reduced chloranil. However, as soon as these latter conditions are met, the rapid dissolution of the reduced chloranil ensues, which in turn leads to a very rapid loss of the electrode capacity.

We also demonstrate that the nature of the metal ion salt used to prepare the aqueous electrolyte can play the role of a proton donor in its hydrated form to compensate for the negative charges of reduced quinones, depending on the Lewis acidity of the metal cation. Furthermore, as these metal ion electrolytes are not buffered, the high local proton consumption during the reduction of a quinone electrode results in the formation of a strong pH gradient, which locally can lead to the precipitation of a metal hydroxide. These different reactivities occurring during the reversible reduction of chloranil- or duroquinone-based electrodes are summarized in Scheme 3.

In light of these results and taking into account the fact that many pK_as of reduced n-type organic compounds are quite basic,[101-104] it is clear that a large number of works are questionable when they report that the charge storage mechanism of n-type organic electrodes in aqueous Zn/organic batteries is based on either the reversible insertion of Zn^{2+} or coinsertion of Zn^{2+} and H^+. Among the few examples of n-type organic compounds that *a priori* allow for reversible insertion of multivalent cations are the naphthalene diimide derivatives.[19, 26] Their theoretical pK_as values calculated by DFT were indeed found to be

quite acidic, leading to pK_a of QH^-/Q^{2-} < 4.0,[105] which is low enough to support charge compensation by cations such as

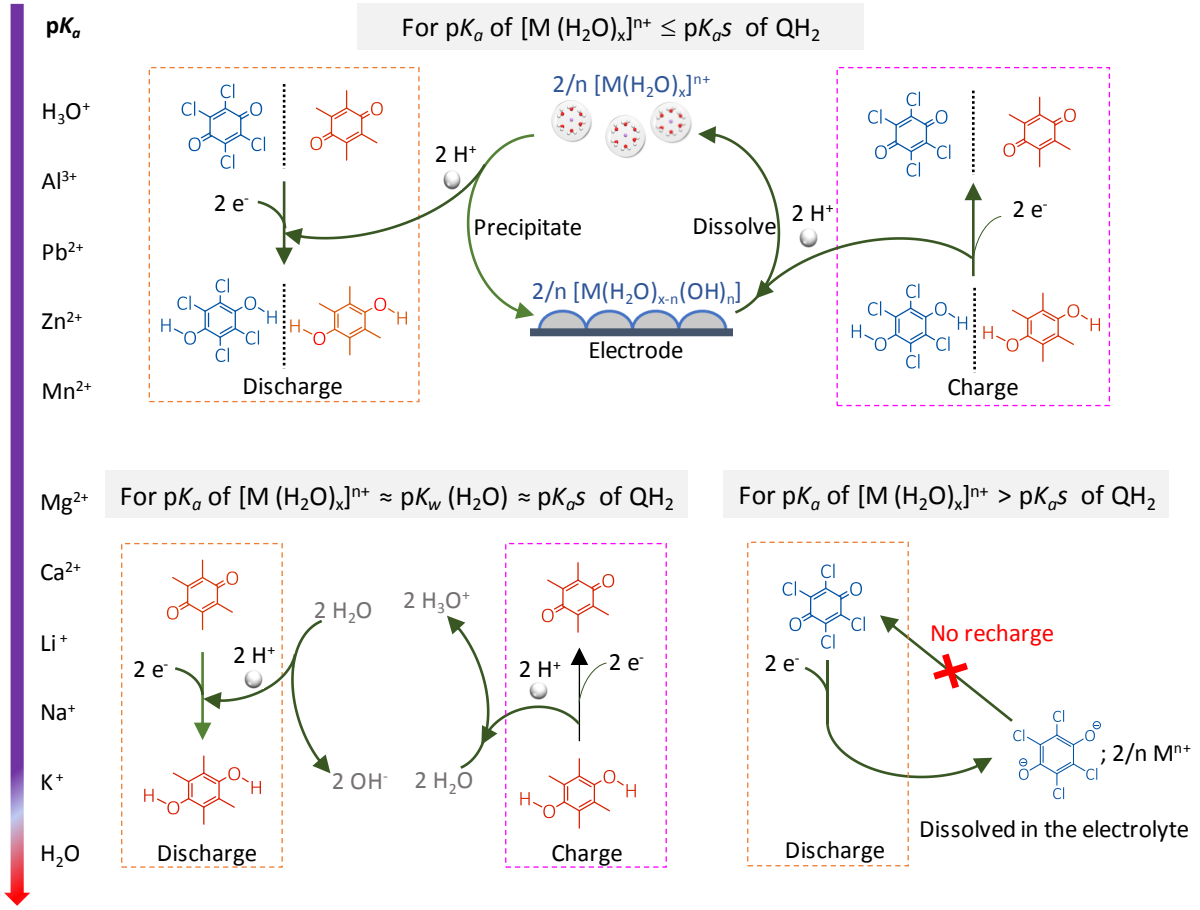

Scheme 3. Schematic summary of the various electrochemical processes that can occur at chloranil- or duroquinone-based electrodes immersed in an unbuffered aqueous metal ion salt electrolyte. The wide arrow on the left indicates the transition from one process to another depending on the nature of the mono- or divalent metal ions used in the electrolyte (and so of pK_a value of the hydrated metal cation).

Ca^{2+} or Zn^{2+}.What could certainly have led to some of the misinterpretations is that, in an unbuffered Zn^{2+}-based mild aqueous electrolyte, the huge amount of protons taken up during the discharge of an n-type organic electrode causes zinc hydroxide to precipitate on top of the electrode surface. The presence of this zinc element on the electrode can easily be misinterpreted as zinc ions inserted in the reduced organic electrode. Another source of misunderstanding is that the Lewis acid character of multivalent metal ions is largely ignored. Indeed, as demonstrated in the present work, when multivalent ions solvate in water, they produce the equivalent of a weak acid capable of supplying protons in the same way as does a weak organic acid.

An important lesson that can be drawn from the above results is that great care must be taken when interpreting the charge storage mechanisms of organic electrodes in protic media, and more specifically of quinone-based electrodes in aqueous electrolytes. Moreover, although we can conclude that multivalent ion insertion cannot take place for a large number of quinones, this does not mean that it is totally unthinkable. As exemplified with the chloranil electrode, the reversible insertion of dications such as Ca^{2+} or Mg^{2+} (which are multivalent metal aquo cations sufficiently weak acidic for being unable to protonate Q^{2-}) is conceivable at pH > 7.0, provided that a cure is found to prevent the dissolution of the reduced quinone. To this end, the incorporation of a quinone moiety (bearing strong electron withdrawing groups in order to have both low pK_as for QH_2 and a high reduction potential for Q) into an insoluble polymer is one possible route.[21, 106] Other possibilities, such as the incorporation of n-type aromatic units into covalent organic framework[107] or through extended conjugation of a quinone moiety into oligomers,[108] are also conceivable.

In view of the universal character of square-scheme PCET mechanisms with regard to quinones and their analogues, but also with regard to many other redox-active organic compounds, the thermodynamic and kinetic analysis we have undertaken here should serve as a guide to the mechanistic charge storage study of many other organic electrodes in aqueous, but also in organic media containing proton donors/acceptors.

4 Experimental Section

4.1 Chemicals

Chloranil, duroquinone , potassium chloride (KCl), manganese chloride ($MnCl_2$), zinc chloride ($ZnCl_2$), aluminum chloride ($AlCl_3$), calcium chloride ($CaCl_2$), sodium chloride (NaCl), lead nitrate ($Pb(NO_3)_2$), dichloroacetic acid ($CHCl_2COOH$), chloroacetic acid

($C_2H_3ClO_2$), acetic acid (CH_3CO_2H), acide phosphorique (H_3PO_4), acide borique ($B(OH)_3$), potassium phosphate (KH_2PO_4), potassium hydroxide (KOH), dimethylformamide (DMF), tetramethylene (THF), carboxymethylcellulose sodium (CMC), polystyrene-block-polybutadiene-block-polystyrene (SBS), Ketjenblack EC-300J, Ketjenblack EC-600JD, and Super P® were purchased from Sigma-Aldrich/Merck. Acetone (Normapur) was purchased from VWR Chemicals. Nafion D-520 dispersion was purchased from Alfa Aesar. All aqueous solutions were made with deionized water (18.2 MΩ cm) and prepared with a TKA MicroPure UV purification system.

4.2 Electrodes preparation

Quinone-based composite electrodes were prepared from slurries obtained as follows. A DMF solution (6 mL) of 300 mg quinone is added dropwise to 200 mL of vigorously stirred deionized water. Next, 175 mg of Super P or Ketjenblack carbon black powder is added under continuous and vigorous stirring for 1 hour. Next, 850 µL of a SBS solution in THF (10 $mg \cdot mL^{-1}$) is slowly injected with a needle into the continuously stirred water suspension over 30 minutes. The resulting mixture is then filtered, rinsed 3 times with water, and then added to a mortar with 16.7 mg CMC dissolved in 2 mL water. After careful mixing, the still-moist slurry is immediately spread on the surface of flat graphite electrodes (purchased from Fisher Scientific™). The thickness and area of the composite are controlled with two layers of a 42 µm adhesive used as a stencil, the surface of the graphite being protected with a supplementary layer of Kimtech™ wipe. The final mass ratio of quinone/carbon/SBS/CMC is 60%:30%:5%:5%. The electrodes are left to air-dry for at least 1 hour. In the case of Super P®-based quinone electrodes, a drop of Nafion solution diluted in ethanol (5 wt. %) is drop-casted on the electrode surface and left to air-dry overnight.

The gravimetric capacity values are referred to the mass of quinone (active component) incorporated in the electrode composite.

4.3 Electrolytes

The buffered electrolytes (0.5 M) were prepared using the following organic and inorganic weak acids, *i.e.* dichloroacetic acid ($CHCl_2COOH$), chloroacetic acid ($C_2H_3ClO_2$), acetic acid (CH_3CO_2H), boric acid ($B(OH)_3$), and potassium phosphate monobasic (KH_2PO_4), to which was added a concentrated solution of KOH in order to adjust the pH to the desired value (*i.e.*, within the buffer zone). An amount of KCl was added to all buffers (except for the phosphate buffer) to adjust the ionic strength to ~0.75 M.

The unbuffered electrolytes (0.5 M) were prepared from dissolution of the following monovalent and divalent metal ion salts in deionized water: potassium chloride (KCl), sodium chloride (NaCl), lithium chloride (NaCl), calcium chloride ($CaCl_2$), magnesium chloride ($MgCl_2$), manganese chloride ($MnCl_2$), zinc chloride ($ZnCl_2$), lead nitrate ($Pb(NO_3)_2$), and aluminum chloride ($AlCl_3$).

4.4 Electrochemical Characterization

Cyclic voltammetry and galvanostatic cycling experiments were performed at room temperature (20-25°C) in a three-electrode cell configuration using a VSP BioLogic potentiostat controlled by EC-Lab software. The counter electrode was a platinum wire and the reference electrode was a saturated calomel electrode (SCE, 0.242 V *vs.* NHE). The electrolyte was carefully degassed for 20 min with argon, and then a constant flow of argon was maintained over the electrolyte for the entire duration of the experiment. In CV, a systematic Ohmic drop compensation was applied. The current density was obtained by normalizing the current intensity to the electrode's geometric area.

4.5 Electrochemical Characterization

SEM images and EDX mapping were collected on a Gemini 360 Scanning Electron Microscope from Zeiss (at an accelerating voltage of 5.0 kV) equipped with an EDX detector from Oxford Instruments (Ultim Max 170 mm^2 detector). The measurements were under a high vacuum. The discharged electrode samples were briefly washed with Milli-Q water to remove remaining salt and left to dry before characterizing by SEM.

For the elemental mapping analysis, the detector has supplier-stated energy resolution at 130 Kcps of: (*i*) Mn Kα resolution less than 127 eV, (*ii*) F Kα resolution less than 64 eV (*iii*) C Kα resolution less than 56 eV. All EDX mapping was obtained by Inlens SE detector (In Column) at 8 kV accelerating voltage. Oxford Instrument AZtec software was used for the acquisition of EDX maps, and point & ID.

4.6 Numerical Simulations

The details for numerical simulations including the models are reported in the Supporting Information.

Associated Content

Supporting Information. Procedures for the numerical simulations of CVs and GDCs; supplementary Figures; and supplementary Tables S1 and S2.

Acknowledgments

We are grateful to the Ile-de-France region and IDEX for the financial support of the AFM-Beam-Rex platform. Thanks to Sarra Derouich for her assistance with SEM and EDX images. The Chinese Scholarship Council is acknowledged for providing Ph.D. funding to Wenkang Wang. We thank Cyrille Costentin for helpful discussions.

6 References

1. Non-metallic charge carriers for aqueous batteries. G. Liang, F. Mo, X. Ji, C. Zhi, *Nat. Rev. Mater.*, **2021**, *6*, 109–123. 10.1038/s41578-020-00241-4
2. Designing modern aqueous batteries. Y. Liang, Y. Yao, *Nat. Rev. Mater.*, **2023**, *8*, 109–122. 10.1038/s41578-022-00511-3
3. Roadmap for advanced aqueous batteries: From design of materials to applications. D. Chao, W. Zhou, F. Xie, C. Ye, H. Li, M. Jaroniec, S-Z. Qiao, *Sci. Adv.*, **2020**, *6*, eaba4098. 10.1126/sciadv.aba4098
4. Opportunities and challenges for organic electrodes in electrochemical energy storage. P. Poizot,, J. Gaubicher, S. Renault, L. Dubois, Y. Liang, Y. Yao, *Chem. Rev.*, **2020**, *120*, 14, 6490–6557. 10.1021/acs.chemrev.9b00482
5. The rise of aqueous rechargeable batteries with organic electrode materials. C. Han, J. Zhu, C. Zhi, H. Li, *J. Mater. Chem. A*, **2020**, *8*, 15479-15512. 10.1039/D0TA03947K
6. Recent advances in aqueous non-metallic ion batteries with organic electrodes. X. Liu, Z. Yang, Y. Lu, Z. Tao, J. Chen, *Small*, **2023**, 2300688. 10.1002/smtd.202300688
7. The emerging aqueous zinc-organic battery. H-G. Wanga, Q. Wub, L. Cheng, G. Zhu, *Coord. Chem. Rev.*, **2022**, *472*, 214772. 10.1016/j.ccr.2022.214772
8. Aqueous zinc batteries: Design principles toward organic cathodes for grid applications. E. Grignon, A. M. Battaglia, T. B. Schon, D. S. Seferos, *iScience*, **2022**, *25*, 104204. 10.1016/j.isci.2022.104204
9. Design strategies for high-performance aqueous Zn/organic batteries. Z. Tie, Z. Niu, *Angew. Chem. Int. Ed.*, **2020**, *59*, 21293–21303. 10.1002/anie.202008960
10. Building better aqueous Zn-organic batteries. Z. Li, J. Tan, Y. Wang, C. Gao, Y. Wang, M. Ye, J. Shen, *Energy Environ. Sci.*, **2023**, *16*, 2398–2431. 10.1039/d3ee00211j
11. Organic materials-based cathode for zinc ion battery. H. Cui, L. Ma, Z. Huang, Z. Chen, C. Zhi, *SmartMat*, **2022**, *3*, 565-581. 10.1002/smm2.1110
12. Recent progress in multivalent metal (Mg, Zn, Ca, and Al) and metal-ion rechargeable batteries with organic materials as promising electrodes. J. Xie, Q. Zhang, *Small*, **2019**, *15*, 1805061. 10.1002/smll.201805061
13. Proton storage chemistry in aqueous zinc-organic batteries: a review. X. Deng, J. K. Sarpong, G. Zhang, J. Hao, X. Zhao, L. Li, H. Li, C. Han, B. Li, *InfoMat*, **2023**, *5*, e12382. 10.1002/inf2.12382
14. High-capacity aqueous zinc batteries using sustainable quinone electrodes. Q. Zhao, W. Huang, Z. Luo, L. Liu, Y. Lu, Y. Li, L. Li,.J. Hu, H. Ma, J. Chen, *Sci. Adv.*, **2018**, *4*, eaao1761. 10.1126/sciadv.aao1761
15. Organic cathode for aqueous Zn-ion batteries: taming a unique phase evolution toward stable electrochemical cycling. D. Kundu, P. Oberholzer, C. Glaros, A. Bouzid, E. Tervoort, A. Pasquarello, M. Niederberger, *Chem. Mater.*, **2018**, *30*, 3874−3881. 10.1021/acs.chemmater.8b01317
16. An environmentally friendly and flexible aqueous zinc battery using an organic cathode. Z. Guo, Y. Ma, X. Dong, J. Huang, Y. Wang, Y. Xia, *Angew. Chem. Int. Ed.*, **2018**, *57*, 11737–11741. https://doi.org/10.1002/anie.201807121
17. Universal quinone electrodes for long cycle life aqueous rechargeable batteries, Y. Liang, Y. Jing, S. Gheytani, K-Y. Lee, P. Liu, A. Facchetti, Y. Yao, *Nat Mater.*, **2017**, *16*, 841-848. 10.1038/nmat4919
18. A quinone electrode with reversible phase conversion for long-life rechargeable aqueous aluminum–metal batteries, J. He, X. Shi, C. Wang, H. Zhang, X. Liu, Z. Yang, X. Lu, *Chem. Commun.*, **2021**, *57*, 6931–6934. 10.1039/D1CC02024B
19. An aqueous Ca-ion battery. S. Gheytani, Y. Liang, F. Wu, Y. Jing, H. Dong, K. K. Rao, X. Chi, F. Fang, Y. Yao, *Adv. Sci.* **2017**, 4, 1700465. 10.1002/advs.201700465
20. Symmetric all-quinone aqueous battery. L. Tong, Y. Jing, R. G. Gordon, M. J. Aziz, *ACS Appl. Energy Mater.*, **2019**, *2*, 4016−4021. 10.1021/acsaem.9b00691
21. An aqueous conducting redox-polymer-based proton battery that can withstand rapid constant-voltage charging and sub-zero temperatures. C. Strietzel, M. Sterby, H. Huang, M. Strømme, R. Emanuelsson, M. Sjödin, *Angew. Chem. Int. Ed.*, **2020**, *59*, 9631–9638. 10.1002/anie.202001191
22. An ultralow temperature aqueous battery with proton chemistry, F. Yue, Z. Tie, S. Deng, S. Wang, M. Yang, Z. Niu, *Angew. Chem. Int. Ed.*, **2021**, *60*, 13882–13886. 10.1002/anie.202103722
23. Designing quinone-based anodes with rapid kinetics for rechargeable proton batteries. X. Yang, Y. Ni, Y. Lu, Q. Zhang, J. Hou, G. Yang, X. Liu, W. Xie, Z. Yan, Q. Zhao, J. Chen, *Angew. Chem. Int. Ed.*, **2022**, e202209642. 10.1002/anie.202209642
24. Co-insertion of water with protons into organic electrodes enables high-rate and high-capacity proton batteries. Z. Su, J. Tang, J. Chen, H. Guo, S. Wu, S. Yin, T. Zhao, C. Jia, Q. Meyer, A. Rawal, J. Ho, Y. Fang, C. Zhao, *Small Struct.*, **2023**, *4*, 2200257. 10.1002/sstr.202200257

25. Aqueous organic hydrogen gas proton batteries with ultrahigh-rate and ultralow-temperature performance. S. Liu, S. Jin, T. Jiang, M. Sajid, J. Xu, K. Zhang, Y. Fan, Q. Peng, X. Zheng, Z. Xie, Z. Liu, Z. Zhu, X. Wang, Q. Nian, J. Chen, K. Li, C. Shen, W. Chen, *Nano Lett.*, **2023**, 23, 20, 9664–9671. 10.1021/acs.nanolett.3c01304
26. Effects of Zn^{2+} and H^{+} association with naphthalene diimide electrodes for aqueous Zn-ion batteries, M. Na, Y. Oh, H. R. Byon, *Chem. Mater.*, **2020**, *32*, 6990−6997. 10.1021/acs.chemmater.0c02357
27. A semi-conductive organic cathode material enabled by extended conjugation for rechargeable aqueous zinc batteries. L. Lin, Z. Lin, J. Zhu, K. Wang, W. Wu, T. Qiu, X. Sun, *Energy Environ. Sci.*, **2023**,*16*, 89-96. 10.1039/D2EE02961H
28. Two-dimensional organic supramolecule via hydrogen bonding and π–π stacking for ultrahigh capacity and long-life aqueous zinc-organic batteries. Y. Chen, J. Li, Q. Zhu, K. Fan, Y. Cao, G. Zhang, C. Zhang, Y. Gao, J. Zou, T. Zhai, C. Wang, *Angew. Chem. Int. Ed.*, **2022**, *61*, e202116289. 10.1002/anie.202116289
29. Orthoquinone-based covalent organic frameworks with ordered channel structures for ultrahigh performance aqueous zinc-organic batteries. S. Zheng, D. Shi, D. Yan, Q. Wang, T. Sun, T. Ma, L. Li, D. He, Z. Tao, J. Chen, *Angew. Chem. Int. Ed.*, **2022**, e202117511. 10.1002/anie.202117511
30. Synergistic co-reaction of Zn^{2+} and H^{+} with carbonyl groups towards stable aqueous zinc–organic batteries. Y. Zhang, C. Zhao, Z. Li, Y. Wang, L. Yan, J. Ma, Y. Wang, *Energy Storage Mater.*, **2022**, *52*, 386–394. 10.1016/j.ensm.2022.08.005
31. A quinoxalinophenazinedione covalent triazine framework for boosted high-performance aqueous zinc-ion batteries. Y. Wang, X. Wang, J. Tanga, W. Tang, *J. Mater. Chem. A*, **2022**, *10*, 13868–13875. 10.1039/D2TA03655J
32. Aqueous multivalent charge storage mechanism in aromatic diamine-based organic electrodes. S. Sariyer, A. Ghosh, S. N. Dambasan, E. M. Halim, M. E. Rhazi, H. Perrot, O. Sel, . R. Demir-Cakan, *ACS Appl. Mater. Interfaces*, **2022**, *14*, 8508–8520. 10.1021/acsami.1c19607
33. Proton insertion chemistry of a zinc-organic battery, Z. Tie, L. Liu, S. Deng, D. Zhao, Z. Niu, *Angew. Chem.*, **2020**, *132*, 4950–4954. 10.1002/ange.201916529
34. A high capacity small molecule quinone cathode for rechargeable aqueous zinc-organic batteries, Z. Lin, H. Y. Shi, L. Lin, X. Yang, W. Wu, X. Sun, *Nat. Commun.*, **2021**, *12*, 4424. 10.1038/s41467-021-24701-9
35. Proton-insertion dominated polymer cathode for high-performance aqueous zinc-ion battery. T. Sun, W. Zhang, Q. Nian, Z. Tao, *Chem. Engineering J.*, **2023**, *452*, 139324. 10.1016/j.cej.2022.139324
36. A Symmetric all-organic proton battery in mild electrolyte. Z. Tie, S. Deng, H. Cao, M. Yao, Z. Niu, J. Chen, *Angew. Chem. Int. Ed.*, **2022**, *61*, e202115180. 10.1002/anie.202115180
37. A carbonyl-rich covalent organic framework as a high-performance cathode material for aqueous rechargeable zinc-ion batteries. D. Ma, H. Zhao, F. Cao, H. Zhao, J. Li, L. Wang, K. Liu, *Chem. Sci.*, **2022**, *13*, 2385–2390. 10.1039/D1SC06412F
38. Binding zinc ions by carboxyl groups from adjacent molecules toward long-life aqueous zinc-organic Batteries. Y. Wang, C. Wang, Z. Ni, Y. Gu, B. Wang, Z. Guo, Z. Wang, D. Bin, J. Ma, Y. Wang, *Adv. Mater.*, **2020**, 2000338. 10.1002/adma.202000338
39. Polyphosphazene based inorganic-organic hybrid cathode containing pyrene tetraone sides for aqueous zinc-ion batteries. S. Sariyer, S. Yeşilot, N. Kılıç, A. Ghosh, O. Sel, R. Demir-Cakan, *Batteries & Supercaps*, **2023**, *6*, e202200529. 10.1002/batt.202200529
40. We have here assumed that $E_{1/2}$ is close to the so-called apparent equilibrium potential E^{0}_{app} (which is here a reasonable approximation in the case of chloranil because the CVs are quite reversible and symmetrical whatever the pH, but of course much less for duroquinone due to the larger peak-to-peak separation and higher CV shape asymmetry (see ref 41).
41. The construction and use of potential-pH diagrams in organic oxidation-reduction reactions. S. I. Bailey, I. M. Ritchie, F. R. Hewgill, *J. Chem. Soc., Perkin Trans. 2*, **1983**, 645−652. 10.1039/P29830000645
42. A cyclic voltammetric study of the aqueous electrochemistry of some quinones. S. I. Bailey, I. M. Ritchie, *Electrochim. Acta*, **1985**, *30*, 3-12. 10.1016/0013-4686(85)80051-7
43. The kinetics and thermodynamics of the reduction of cytochrome c by substituted p-benzoquinols in solution. P. R. Rich, D. S. Bendall, *Biochim. Biophys. Acta*, **1980**, *592*, 506−518. 10.1016/0005-2728(80)90095-X
44. Modulation of quinone PCET reaction by Ca^{2+} ion captured by calix[4]quinone in water. Y-R. Kim, R. S. Kim, S. K. Kang, M. G. Choi, H. Y. Kim, D. Cho, J. Y. Lee, S-K. Chang, T. D. Chung, *J. Am. Chem. Soc.*, **2013**, *135*, 18957−18967. 10.1021/ja410406e
45. Hydrogen-bonding and protonation effects in electrochemistry of quinones in aprotic solvents. N. Gupta, H. Linschitz, *J. Am. Chem. Soc.* **1997**, *119*, 6384−6391. 10.1021/ja970028j

46. Voltammetry of quinones in unbuffered aqueous solution: reassessing the roles of proton transfer and hydrogen bonding in the aqueous electrochemistry of quinones. M. Quan, D. Sanchez, M. F. Wasylkiw, D. K. Smith, *J. Am. Chem. Soc.*, **2007**, *129*, 12847−12856. 10.1021/ja0743083
47. Electrochemical reduction of quinones in different media. P. S. Guin, S. Das, P. C. Mandal, *Int. J. Electrochem.*, **2011**, *2011*, 1−22. 10.4061/2011/816202
48. The ionization constants of some hydroquinones. Baxendale J. H., Hardy H. R. *Trans. Faraday Soc.*, **1953**, *49*, 1140. 10.1039/tf9534901140
49. Electrochemical reactions with protonations at equilibrium: Part VIII. The 2 e, 2 H^+ reaction (nine-member square scheme) for a surface or for a heterogeneous reaction in the absence of disproportionation and dimerization reactions. E. Laviron, *J. Electroanal. Chem.*, **1983**, *146*, 15−36. 10.1016/S0022-0728(83)80110-7
50. Electrochemistry of quinones. J. Q. Chambers in The quinonoid compounds, Eds: Patai S., Rappoport Z., 1988, Chapter 12, pp 719−757. 10.1002/9780470772119.ch12
51. Update 1 of: Electrochemical approach to the mechanistic study of proton-coupled electron transfer. C. Costentin, M. Robert, J-M. Savéant, *Chem. Rev.*, **2010**, *110*, PR1–PR40. 10.1021/cr100038y
52. Electrochemical reactions with protonations at equilibrium: Part XII. The 2 e^-, 2 H^+ homogeneous isotopic electron exchange reaction (nine-member square scheme). E. Laviron, *J. Electroanal. Chem.*, **1984**, *169*, 29-46.
53. Equilibria of substituted semiquinones at high pH. Bishop C. A., Tong L. K. J., *J. Am. Chem. Soc.*, **1965**, *87*, 501-505. 10.1021/ja01081a018
54. Short-lived phenoxy- and semiquinone radicals. I. V. Khudyakov, V. A. Kuz'min, *Russ. Chem. Rev.*, **1975**, *44*, 801–8014. 10.1070/RC1975v044n10ABEH002377
55. Semiquinone free radicals: determination of acid dissociation constants by pulse radiolysis. Willson R. L., *Trans. Faraday Soc.*, **1971**, *67*, 3020. 10.1039/C29710001249
56. Ionization constants and spectral characteristics of some semiquinone radicals in aqueous solution. Rao, P. S.; Hayon, E. *J. Phys. Chem.*, **1973**, *77*, 2274–2276. 10.1021/j100638a003
57. Electron transfer rates and equilibriums between substituted phenoxide ions and phenoxyl radicals. S. Steenken, P. Neta, *J. Phys. Chem.*, **1979**, *83*, 1134−1137. 10.1021/j100472a005
58. ECE and disproportionation: Part VI. General resolution. Application to potential step chronoamperometry. C Amatore, J-M. Savéant, *J. Electroanal. Chem.*,**1979**, *102*, 21. 10.1016/S0022-0728(79)80026-1
59. The assumption of using a same k^0 value for chloranil is reasonable insofar as the single or two reversible waves remains highly symmetrical and reversible whatever the pH. Moreover, the two reversible waves of chloranil at high pH, characterizing the two sequential pure one-electron transfer, could be well fitted with simulated CV using an ET rate constant of 1 cm/s.
60. Electrochemical reactions with protonations at equilibrium: Part X. The kinetics of the p-benzoquinone/hydroquinone couple on a platinum electrode. E. Laviron, *J. Electroanal. Chem.*, **1984**, *164*, 213−227. 10.1016/S0022-0728(84)80207-7
61. Proton coupled electron transfer of ubiquinone Q_2 incorporated in a self-assembled monolayer. C. Lemmer, M. Bouvet, R. Meunier-Prest, *Phys. Chem. Chem. Phys.*, **2011**, *13*, 13327–13332. 10.1039/c0cp02700f
62. The kinetics of some substituted catechol/o-quinones couples at a carbon paste electrode. M. R. Deakin, R. M. Wightman, *J. Electroanal. Chem.*, **1986**, *206*, 167−177. 10.1016/0022-0728(86)90266-4
63. It is to note that by analogy with duroquinone, we have assumed that the p$K_{a,1}$ and p$K_{a,4}$ values of chloranil are so much acidic that their contribution can be considered as negligible within the pH range investigated (meaning that the species QH^+ and QH_2^{2+} can be removed from the simulations, appearing thus in light gray in Figure 1d). The same reasoning was thus applied for duroquinone, where the p$K_{a,4}$ was considered so low that reactions relevant to the QH_2^{2+} species could be removed from simulations (Figure 1h).
64. Electrochemistry of potentially bioreductive alkylating quinones: Part 3. Quantitative structure-electrochemistry relationships of aziridinylquinones. R. J. Driebergen, E. E. Moret, L. H. M. Janssen, J. S. Blauw, J. J. M. Holthuis, S. J. P. Kelder, W. Verboom, D. N. Reinhoudt, W. E. Vanderlinden, *Anal. Chim. Acta*, **1992**, *257*, 257–273. 10.1016/0003-2670(92)85179-A
65. Evaluation of organic battery electrodes: Voltammetric study of the redox behaviour of solid quinones, H. Alt, H. Binder, G. Klempert, A. Köhling, G. Sandstede, *J. Appl. Electrochem.*, **1972**, *2*, 193. 10.1007/BF02354976
66. Electrochemical and X-ray diffraction study of the redox cycling of nanocrystals of 7,7,8,8-tetracyanoquinodimethane. Observation of a solid-solid phase transformation controlled by nucleation and growth. A. M. Bond, S. Fletcher, F. Marken, S. J. Shaw, P. G. Symons, *J. Chem. Soc. Faraday Trans.*, **1996**; *92*, 3925–3933. 10.1039/FT9969203925

67. Theory for double potential step chronoamperometry, chronocoulometry, and chronoabsorptometry with a quasi-reversible electrode reaction. D. H. Evans, M. J. Kelly, Anal. Chem., **1982**, *54*, 1727−1729. 10.1021/ac00248a016
68. Hysteresis in electrochemical systems. A. Van der Ven, K. A. See, L. Pilon, *Battery Energy*, **2022**, *1*, 20210017. 10.1002/bte2.20210017
69. Square-scheme electrochemistry in battery electrodes. M. Okubo, K. Kawai, Z. Ma, A. Yamada, *Acc. Mater. Res.*, **2022**, *3*, 33−41. 10.1021/accountsmr.1c00155
70. Two-phase transition of Li-intercalation compounds in Li-ion batteries. D. Li, H. Zhou, *Mater. Today*, **2014**, *17*, 451−463. 10.1016/j.mattod.2014.06.002
71. Fictitious phase separation in Li layered oxides driven by electro-autocatalysis. J. Park, H. Zhao, S. D. Kang, K. Lim, C-C. Chen, Y-S. Yu, R. D. Braatz, D. A. Shapiro, J. Hong, M. F. Toney, M. Z. Bazant, W. C. Chueh, *Nat. Mater*., **2021**, *20*, 991–999. 10.1038/s41563-021-00936-1
72. Two-phase electrochemical proton transport and storage in a-MoO3 for Proton Batteries. H. Guo, D. Goonetilleke, N. Sharma, W. Ren, Z. Su, A. Rawal, C. Zhao, *Cell Rep. Phys. Sci.*, **2020**, *1*, 100225. 10.1016/j.xcrp.2020.100225
73. Phase transition mechanism for crystalline aromatic dicarboxylate in Li^+ intercalation. R. Mikita, N. Ogihara, N. Takahashi, S.Kosaka, N. Isomura, *Chem. Mater.*, **2020**, *32*, 3396−3404. 10.1021/acs.chemmater.9b04984
74. Insights into redox processes and correlated performance of organic carbonyl electrode materials in rechargeable batteries. Y. Lu, Y. Cai, Q. Zhang, J. Chen, *Adv. Mater.*, **2022**, *34*, 2104150. 10.1002/adma.202104150
75. Electrochemical methods: fundamentals and applications. A.J. Bard and L.R. Faulkner, Edition, John Wiley & Sons, New York, 2nd ed., 2001.
76. Insights into the cyclic voltammetry of surface-confined molecules undergoing two-electron transfers of any reversibility and any ordering of the formal potentials: unravelling the apparent governing factors. M. López-Tenés, J. González, E. Laborda, A. Molina, *Electrochim. Acta*, **2023**, *462*, 142694. 10.1016/j.electacta.2023.142694
77. Electrochemical energy storage: questioning the popular $v/v^{1/2}$ scan rate diagnosis in cyclic voltammetry. C. Costentin, *J. Phys. Chem. Lett.* **2020**, *11*, 9846−9849. 10.1021/acs.jpclett.0c02667
78. Capacitive and diffusive contributions in supercapacitors and batteries: A critique of b-value and the v-$v^{1/2}$ model. S. Pervez, M. Z. Iqbal, *Small* **2023**, *19*, 2305059. 10.1002/smll.202305059
79. Cyclic voltammetry modeling of proton transport effects on redox charge storage in conductive materials: application to a TiO_2 mesoporous film. Y. S. Kim, V. Balland, B. Limoges, C. Costentin, *Phys. Chem. Chem. Phys.*, **2017**, *19*, 17944−17951. 10.1039/C7CP02810E
80. Diffusion in dilute aqueous acetic acid solutions at 25°C. D. G. Leaist, P. A. Lyons, *J. Solution Chem.*, **1984**, *13*, 77–85. 10.1007/BF00646041
81. Proton transfer and the mobilities of the H^+ and OH^- ions from studies of a dissociating model for water. H. L. Song, C. R. Jayendran, *J. Chem. Phys.*, **2011**, *135*, 124505. 10.1063/1.3632990
82. Self-diffusion coefficients and rotational correlation times in polar liquids. II. D. E. O'Reilly, E. M. Peterson. *J. Chem. Phys.*, **1971**, *55*, 2155–2163. 10.1063/1.1676386
83. Diffuse charge and faradaic reactions in porous electrodes. P. M. Biesheuvel, Y. Q. Fu, M. Z. Bazant, *Phys. Rev. E*, **2011**, *83*, 061507. 10.1103/PhysRevE.83.061507
84. Effective self-diffusivity and the concept of tortuosity. M. R. Bonilla, S. K. Bhatia, *J. Phys. Chem. C*, **2012**, *117*, 3343−3357. 10.1021/jp3070954
85. Fogler, H. S. Elements of chemical reaction engineering; Prentice Hall PTR: Upper Saddle River, NJ, 2002.
86. Theoretical analysis of current distribution in porous electrodes. J. S. Newman, C. W. Tobias, *J. Electrochem. Soc.* **1962**, *109*, 1183−1191. 10.1149/1.2425269
87. Organic electrode materials for fast-rate, high-power battery applications. C. N. Gannett, L. Melecio-Zambrano, M. J. Theibault, B. M. Peterson, B. P. Fors, H. D. Abruna, *Mater. Rep.: Energy*, **2021**, 1, 100008. 10.1016/j.matre.2021.01.003
88. The other factors which might also influence the voltammetric behavior of the solid-state quinones are the non-ideality of the medium, which may require considering the possible molecular interactions between the different redox species, but also the dismutation/comproportionation reactions which can no longer be considered as negligible.
89. Cyclic voltammetry to study dynamics of ion insertion in porous materials. C. Costentin, *Adv. Energy Sustainability Res.*, **2024**, *5*, 2300242. 10.1002/aesr.202300242
90. On the unsuspected role of multivalent metal ions on the charge storage of a metal oxide electrode in mild aqueous electrolytes. Y.-S. Kim, K. D. Harris, B. Limoges, V. Balland, *Chem. Sci.* **2019**, *10*, 8752. 10.1039/C9SC02397F

91. Multivalent-ion versus proton insertion into nanostructured electrochromic WO_3 from mild aqueous electrolytes. T. Rocca, A. Gurel, D. Schaming, B. Limoges, V. Balland, *ACS Appl. Mater. Interfaces*, **2024,** *16* (18), 23567–23575. 10.1021/acsami.4c02152
92. Accessing the two-electron charge storage capacity of MnO_2 in mild aqueous electrolytes. M. Mateos, N. Makivic, Y.-S. Kim, B. Limoges, V. Balland, *Adv. Energy Mater.*, **2020**, *10*, 2000332. 10.1002/aenm.202000332
93. The role of Al^{3+}-based aqueous electrolytes in the charge storage mechanism of MnO_x cathodes. V. Balland, M. Mateos, A. Singh, K. D. Harris, C. Laberty-Robert, B. Limoges, *Small* **2021**, *17*, 2101515. 10.1002/smll.202101515
94. Nanostructured electrode enabling fast and fully-reversible MnO_2-to-Mn^{2+} conversion in mild buffered aqueous electrolytes. M. Mateos, K. D. Harris, B. Limoges, V. Balland. *ACS Appl. Energy Mater.*, **2020**, *3*, 7610–7618. 10.1021/acsaem.0c01039
95. Challenging metal-ion rocking-chair and zinc-ion mechanisms in mild acidic to neutral aqueous electrolytes. A. Singh, Da. Grenz, Y. Pellegrin, F. Odobel, P. Poizot, J. Gaubicher, *Electrochem. Commun.* **2023**, *154*, 107559. 10.1016/j.elecom.2023.107559
96. All positive ions give acid solutions in water. S. J. Hawkes, *J. Chem. Educ.* **1996**, *73*, 516. 10.1021/ed073p516
97. It is to note that a same discrepancy between simulation and experiment is observed for the buffered electrolytes in the same pH range (Figure 1F), indicating that the main issue lies in the difficulty we had in accurately describing the full kinetics of the duroquinone square scheme mechanism.
98. Impact of reversible proton insertion on the electrochemistry of electrode materials operating in mild aqueous electrolytes: a case study with TiO_2. N. Makivić, K. D. Harris, J-M. Tarascon, B. Limoges, V. Balland, *Adv. Energy Mater.*, **2023,** *3*, 2203122. 10.1002/aenm.202203122
99. The calculation of the solubility of metal hydroxides, oxide-hydroxides, and oxides, and their visualisation in logarithmic diagrams. S. Fritz, K. Heike, *ChemTexts*, **2015**, *1*, 7. 10.1007/s40828-015-0006-0
100. The metal hydroxide accumulated over the electrode plays a role equivalent to a local base reservoir which, during the reverse scan, can be used to neutralize protons released by the electrooxidation of QH_2, thus keeping the local pH relatively stable until the insoluble metal hydroxide is fully dissolved (behaving thus as a buffering agent).
101. Predicting pK_a values of quinols and related aromatic compounds with multiple OH groups. M. Morency, S. Néron, R. Iftimie, J. D. Wuest, *J. Org. Chem.*, **2021**, *86*, 14444−14460. 10.1021/acs.joc.1c01279
102. Prediction of Pourbaix diagrams of quinones for redox flow battery by COSMO-RS. T. Gaudin, J-M. Aubry, *J. Energy Storage*, **2022**, *49*, 104152. 10.1016/j.est.2022.104152
103. Density functional theory and machine learning for electrochemical square-scheme prediction: an application to quinone-type molecules relevant to redox flow batteries. A. Hashemi, R. Khakpour, A. Mahdian, M. Busch, P. Peljo, K. Laasonen, *Digital Discovery*, **2023**, *2*, 1565–1576. 10.1039/D3DD00091E
104. pH dependent electrochemical characterization, computational studies and evaluation of thermodynamic, kinetic and analytical parameters of two phenazines. A. H. Shah, W. Zaid, A. Shah, U. A. Rana, H. Hussain, M. N. Ashiq, R. Qureshi, A. Badshah, M. A. Zia, He-B. Kraatz, *J. Electrochem. Soc.*, **2015**, *162*, H115−H123. 10.1149/2.0481503jes
105. The electrochemical response of core-functionalized naphthalene diimides (NDI) –a combined computational and experimental investigation. C. Wiberg, M. Busch, L. Evenäs, E. Ahlberg, *Electrochim. Acta*, **2021**, *367*, 137480. 10.1016/j.electacta.2020.137480
106. An ultrahigh performance zinc-organic battery using poly(catechol) cathode in $Zn(TFSI)_2$-based concentrated aqueous electrolytes, N. Patil, C. de la Cruz, D. Ciurduc, A. Mavrandonakis, J. Palma, R. Marcilla, *Adv. Energy Mater.*, **2021**, 2100939. 10.1002/aenm.202100939
107. Covalent organic frameworks as model materials for fundamental and mechanistic understanding of organic battery design principles. S. Haldar, A. Schneemann, S. Kaskel, *J. Am. Chem. Soc.*, **2023**, *145*, 13494−13513. 10.1021/jacs.3c01131
108. High-rate, high-capacity electrochemical energy storage in hydrogen-bonded fused aromatics, T. Chen, H. Banda, L. Yang, J. Li, Y. Zhang, R. Parenti, M. Dincă, *Joule*, **2023**, *7*, 986−1002. 10.1016/j.joule.2023.03.011

Supporting Information

A unified charge storage mechanism to rationalize the electrochemical behavior of quinone-based organic electrodes in aqueous rechargeable batteries

Wenkang Wang, Véronique Balland, Mathieu Branca and Benoît Limoges**

Université Paris Cité, CNRS, Laboratoire d'Electrochimie Moléculaire, F-75013 Paris, France.

E-mails: mathieu.branca@u-paris.fr ; limoges@u-paris.fr

Numerical Simulations

A standard semi-infinite one-compartment 1D model (see Scheme 1) was used for numerical simulations of the CVs of quinones in homogeneous solution (the length δ of this compartment representing the electrolyte domain was chosen as a multiple of the diffusion-convection layer thickness in order to have almost no alteration of the bulk concentrations at this δ boundary), while a finite/semi-infinite two-compartment 1D model (see Scheme 1, based on a first finite compartment of thickness L to represent the porous quinone-based electrode domain, juxtaposed to a second semi-infinite compartment of length δ to define the electrolyte domain) was selected for numerical simulations of the GDC profiles (this two-compartment model is in line to the one we had previously described in ref S1).

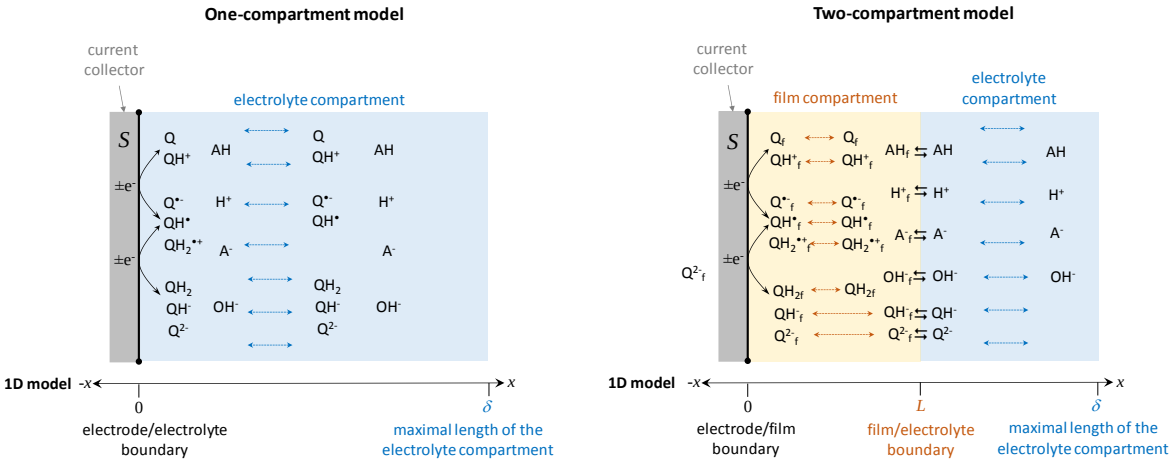

Scheme S1. Schematic representation of (left) the semi-infinite one-compartment 1D model and (right) finite/semi-infinite two-compartment 1D model.

For both models, the mass transport of species in the electrolyte compartment (or domain) was assumed to occur by linear semi-infinite diffusion-convection perpendicular to the electrode's geometric area *S*, while for the two-compartment 1D model the redox-active species (*i.e.*, the quinones and their different reduced states) as well as the electrolyte components also present in the electrode domain were considered to be homogeneously

distributed within the finite thickness *L* (100 µm) and capable to freely diffuse, isotropically, across this finite thickness. In addition, for modeling the protonation steps not only in the electrolyte compartment but also within the electrode domain, the overall proton donor/proton acceptor couples were considered with their overall possible acid/base equilibrium reactions (see below). In the case of the two-compartment 1D model, the overall proton donor/proton acceptor couples present in the electrode domain (*i.e.*, at a same concentration than in the electrolyte compartment) were considered to freely and rapidly distribute between the two compartments by applying for each species a partitioning coefficient equal to 1 and k_{on} and k_{off} partitioning rate constants of 0.1 s^{-1} at the boundary of the two compartments. Furthermore, due to the high ionic strength of the aqueous electrolytes, it was assumed that the contribution of migration to the charge carrier mass transfer could be neglected. Also, for all species the activities were assimilated to concentrations.

For modeling the square scheme mechanism of each quinone in either the electrolyte or electrode compartment, we have at first considered that the nine-member square scheme can be simplified by an eight-member square scheme because the contribution of QH_2^{2+} is negligible within the pH range explored. It thus leads to the following overall set of possible reactions:

i) at the boundary electrode/electrolyte interface (source terms at x = 0), the following set of elementary electron transfer reactions:

$Q + e^- \rightleftarrows Q^{\bullet -}$ $\quad E_1^0,\ k_1^0,\ \alpha_1$

$Q^{\bullet -} + e^- \rightleftarrows Q^{2-}$ $\quad E_2^0,\ k_2^0,\ \alpha_2$

$QH^+ + e^- \rightleftarrows QH^{\bullet}$ $\quad E_3^0,\ k_3^0,\ \alpha_3$

$QH^{\bullet} + e^- \rightleftarrows QH^-$ $\quad E_4^0,\ k_4^0,\ \alpha_4$

$QH_2^{\bullet+} + e^- \rightleftarrows QH_2$ $\quad E_6^0,\ k_6^0,\ \alpha_6$

ii) in the electrolyte or electrode compartment, the following acid-base equilibriums:

(those involving the H_3O^+/H_2O proton donor/proton acceptor couple)

$QH^+ \rightleftarrows Q + H^+$ with $K_{a,1} = \frac{k_{1,d}}{k_{1,p}} = 10^{-pH}\frac{C_Q}{C_{QH^+}} = 10^{-pK_{a,1}}$

$QH^{\bullet} \rightleftarrows Q^{\bullet-} + H^+$ with $K_{a,2} = \frac{k_{2,d}}{k_{2,p}} = 10^{-pH}\frac{C_{Q^{\bullet-}}}{C_{QH^{\bullet}}} = 10^{-pK_{a,2}}$

$QH^- \rightleftarrows Q^{2-} + H^+$ with $K_{a,3} = \frac{k_{3,d}}{k_{3,p}} = 10^{-pH}\frac{C_{Q^{2-}}}{C_{QH^-}} = 10^{-pK_{a,3}}$

$QH_2^{\bullet+} \rightleftarrows QH^{\bullet} + H^+$ with $K_{a,5} = \frac{k_{5,d}}{k_{5,p}} = 10^{-pH}\frac{C_{QH^{\bullet}}}{C_{QH_2^{\bullet+}}} = 10^{-pK_{a,5}}$

$QH_2 \rightleftarrows QH^- + H^+$ with $K_{a,6} = \frac{k_{6,d}}{k_{6,p}} = 10^{-pH}\frac{C_{QH^-}}{C_{QH_2}} = 10^{-pK_{a,6}}$

where $k_{i,d}$ and $k_{i,p}$ are the dissociation (in s^{-1}) and protonation (in $M^{-1}\ s^{-1}$) rate constants of the i subscript reaction.

(those involving the AH/A^- proton donor/proton acceptor couple from the buffer)

$AH \rightleftarrows A^- + H^+$ with $K_a = \frac{k_{AH,d}}{k_{AH,p}} = 10^{-pH}\frac{C_{A^-}}{C_{AH}} = 10^{-pK_a}$

$QH^{\bullet} + A^- \rightleftarrows Q^{\bullet-} + AH$ with $K_{eq,7} = \frac{k_7}{k_{-7}} = \frac{K_{a,2}}{K_a}$

$Q^{2-} + AH \rightleftarrows QH^{-} + A^{-}$ with $K_{eq,8} = \frac{k_8}{k_{-8}} = \frac{K_a}{K_{a,3}}$

$QH^{-} + AH \rightleftarrows QH_2 + A^{-}$ with $K_{eq,9} = \frac{k_9}{k_{-9}} = \frac{K_a}{K_{a,6}}$

$QH^{+} + A^{-} \rightleftarrows Q + AH$ with $K_{eq,10} = \frac{k_{10}}{k_{-10}} = \frac{K_{a,1}}{K_a}$

$QH_2^{\bullet+} + A^{-} \rightleftarrows QH^{\bullet} + AH$ with $K_{eq,11} = \frac{k_{11}}{k_{-11}} = \frac{K_{a,5}}{K_a}$

where k_i and k_{-i} are the forward and backward proton exchange rate constants (in M^{-1} s^{-1}) of the i subscript reaction.

(those involving the H_2O/OH^- proton donor/proton acceptor couple)

$H_2O \rightleftarrows OH^{-} + H^{+}$ with $K_w = \frac{k_{w,d}}{k_{w,p}} = C_{OH^-} C_{H_3O^+} = 10^{-pK_w}$

$QH^{-} + OH^{-} \rightleftarrows Q^{2-} + H_2O$ with $K_{eq,12} = \frac{k_{12}}{k_{-12}} = \frac{K_{a,3}}{K_w}$

$QH_2 + OH^{-} \rightleftarrows QH^{-} + H_2O$ with $K_{eq,13} = \frac{k_{13}}{k_{-13}} = \frac{K_{a,6}}{K_w}$

$QH^{\bullet} + OH^{-} \rightleftarrows Q^{\bullet-} + H_2O$ with $K_{eq,14} = \frac{k_{14}}{k_{-14}} = \frac{K_{a,2}}{K_w}$

$QH^{+} + OH^{-} \rightleftarrows Q + H_2O$ with $K_{eq,15} = \frac{k_{15}}{k_{-15}} = \frac{K_{a,1}}{K_w}$

$QH_2^{\bullet+} + OH^{-} \rightleftarrows QH^{\bullet} + H_2O$ with $K_{eq,16} = \frac{k_{16}}{k_{-16}} = \frac{K_{a,5}}{K_w}$

iii) in the electrolyte or electrode compartment, the following acid-base equilibrium exchanges between the quinone species themselves:

$\mathrm{QH^+ + QH^- \rightleftarrows Q + QH_2}$ with $K_{eq,17} = \frac{k_{17}}{k_{-17}} = \frac{K_{a,1}}{K_{a,6}}$

$\mathrm{QH^+ + Q^{2-} \rightleftarrows Q + QH^-}$ with $K_{eq,18} = \frac{k_{18}}{k_{-18}} = \frac{K_{a,1}}{K_{a,3}}$

$\mathrm{QH_2^{\bullet+} + Q^{2-} \rightleftarrows QH^{\bullet} + QH^-}$ with $K_{eq,19} = \frac{k_{19}}{k_{-19}} = \frac{K_{a,5}}{K_{a,3}}$

$\mathrm{QH^{\bullet} + Q^{2-} \rightleftarrows Q^{\bullet-} + QH^-}$ with $K_{eq,20} = \frac{k_{20}}{k_{-20}} = \frac{K_{a,2}}{K_{a,3}}$

$\mathrm{QH_2 + Q^{2-} \rightleftarrows QH^- + QH^-}$ with $K_{eq,21} = \frac{k_{21}}{k_{-21}} = \frac{K_{a,6}}{K_{a,3}}$

$\mathrm{QH_2^{\bullet+} + Q^{\bullet-} \rightleftarrows QH^{\bullet} + QH^{\bullet}}$ with $K_{eq,22} = \frac{k_{22}}{k_{-22}} = \frac{K_{a,5}}{K_{a,2}}$

$\mathrm{QH_2^{\bullet+} + QH^- \rightleftarrows QH^{\bullet} + QH_2}$ with $K_{eq,23} = \frac{k_{23}}{k_{-23}} = \frac{K_{a,5}}{K_{a,6}}$

$\mathrm{QH^+ + Q^{\bullet-} \rightleftarrows Q + QH^{\bullet}}$ with $K_{eq,24} = \frac{k_{24}}{k_{-24}} = \frac{K_{a,1}}{K_{a,2}}$

$\mathrm{QH^+ + QH^{\bullet} \rightleftarrows Q + QH_2^{\bullet+}}$ with $K_{eq,25} = \frac{k_{25}}{k_{-25}} = \frac{K_{a,1}}{K_{a,5}}$

iii) in the electrolyte or electrode compartment, the following disproportionation/comproportionation equilibrium reactions:

$\mathrm{Q^{\bullet-} + Q^{\bullet-} \rightleftarrows Q + Q^{2-}}$ with $K_{\mathrm{dis},1} = \frac{k_{\mathrm{dis},1}}{k_{\mathrm{co},1}} = \exp\left[-\frac{F}{RT}\left(E_1^0 - E_2^0\right)\right]$

$QH^{\bullet} + QH^{\bullet} \rightleftarrows QH^{+} + QH^{-}$ with $K_{dis,2} = \frac{k_{dis,2}}{k_{co,2}} = \exp\left[-\frac{F}{RT}\left(E_3^0 - E_4^0\right)\right]$

$Q^{\bullet-} + QH_2^{\bullet+} \rightleftarrows Q + QH_2$ with $K_{dis,3} = \frac{k_{dis,3}}{k_{co,3}} = \exp\left[-\frac{F}{RT}\left(E_1^0 - E_6^0\right)\right]$

$Q^{\bullet-} + QH^{\bullet} \rightleftarrows Q + QH^{-}$ with $K_{dis,4} = \frac{k_{dis,4}}{k_{co,4}} = \exp\left[-\frac{F}{RT}\left(E_1^0 - E_4^0\right)\right]$

$QH^{\bullet} + Q^{\bullet-} \rightleftarrows QH^{+} + Q^{2-}$ with $K_{dis,5} = \frac{k_{dis,5}}{k_{co,5}} = \exp\left[-\frac{F}{RT}\left(E_3^0 - E_2^0\right)\right]$

$QH^{\bullet} + QH_2^{\bullet+} \rightleftarrows QH^{+} + QH_2$ with $K_{dis,6} = \frac{k_{dis,6}}{k_{co,6}} = \exp\left[-\frac{F}{RT}\left(E_3^0 - E_6^0\right)\right]$

where $k_{dis,i}$ and $k_{co,i}$ are the disproportionation and comproportionation rate constants (in M^{-1} s^{-1}) of the i subscript reaction. Whether or not these equilibrium reactions are added to the simulations, it was observed that they do not significantly change the results.

For simulations, all protonation rate constants involving the free protons as reactant, *i.e.* $k_{i,p}$, $k_{AH,p}$, and $k_{w,p}$, were assumed to be under diffusion control and so all governed by a same high maximal rate constant value of 10^{10} M s^{-1}. For the other protonation rate constants, we have considered that when the equilibrium constant $K_{eq,i}$ is > 1, the forward rate constant k_i of the reaction i is under diffusion control with a value of 10^9 M s^{-1}, while when $K_{eq,i}$ < 1 this is the reverse rate constant k_{-i} that is under diffusion control and so equal to 10^9 M s^{-1}. For the disproportionation/comproportionation rate constants, we have applied the same reasoning, *i.e.* when the dismutation equilibrium constant $K_{dis,i}$ is > 1, the disproportionation rate constant of the reaction i is considered under diffusion control with a value $k_{dis,i} = 10^8$ M s^{-1}, while when $K_{dis,i}$ < 1 this is $k_{co,i}$ that is equal to 10^8 M s^{-1}.

An additional source term included to the model at $x = 0$ is the capacitive current arising from the charging/discharging of the double-layer capacitance of either the glassy carbon electrode (C_{dl} = 30 μF·cm^{-2}) used for CV experiments in homogeneous solution or of the highly porous quinone-based composite electrodes ($C_{dl} = 10^5$ μF·cm^{-2}) used for GDC experiments.

For simulations of the galvanostatic charges/discharges, the following conditions were applied:

$0 < t < t_{inv}$: at $x = 0$, $i = -i_g$ (charge)

$t_{inv} < t < t_{max}$: at $x = 0$, $i = i_g$ (discharge)

where i is the total current imposed on the electrode, i_g the imposed current rate, and t_{inv} the time where the charge or discharge is inverted to discharge or charge, respectively.

At $t = 0$ and $x = 0$, the initial potential (open-circuit potential) of the electrode is given by:

$$E_i = \frac{E^0_{A/B,app} + E^0_{B/C,app}}{2} + \frac{RT}{2F} \ln\left(\frac{1-\theta_i}{\theta_i}\right)$$

where θ_i is the fraction of the fully reduced form of quinone in the composite electrode. An arbitrarily low value of 10^{-6} was selected in order to avoid an indefinite E_i value.

Because of the slow rates we have used, the effect of the Ohmic drop on the potential was considered to be negligible.

The above two models were numerically simulated by finite element analysis using COMSOL Multiphysics software (v. 5.5) on a PC computer with Intel Xeon E-2236 CPU, 32 GB RAM and Windows 10 Pro operating system.

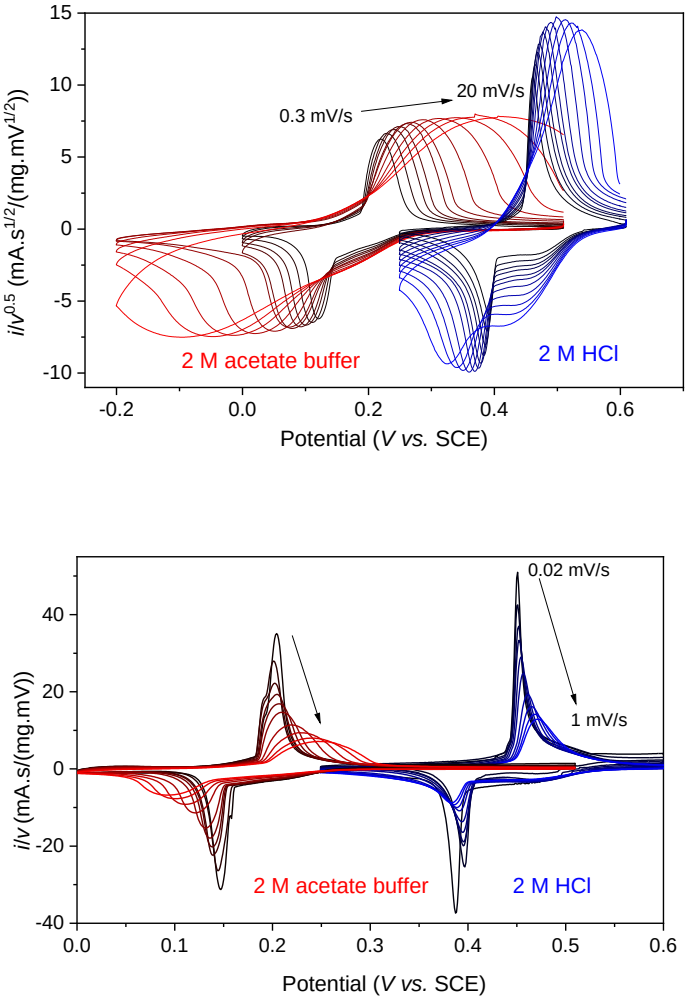

Figure S1. Same CVs than in Figure 2e but normalized to (top) $\sqrt{v}$ and (bottom) v.

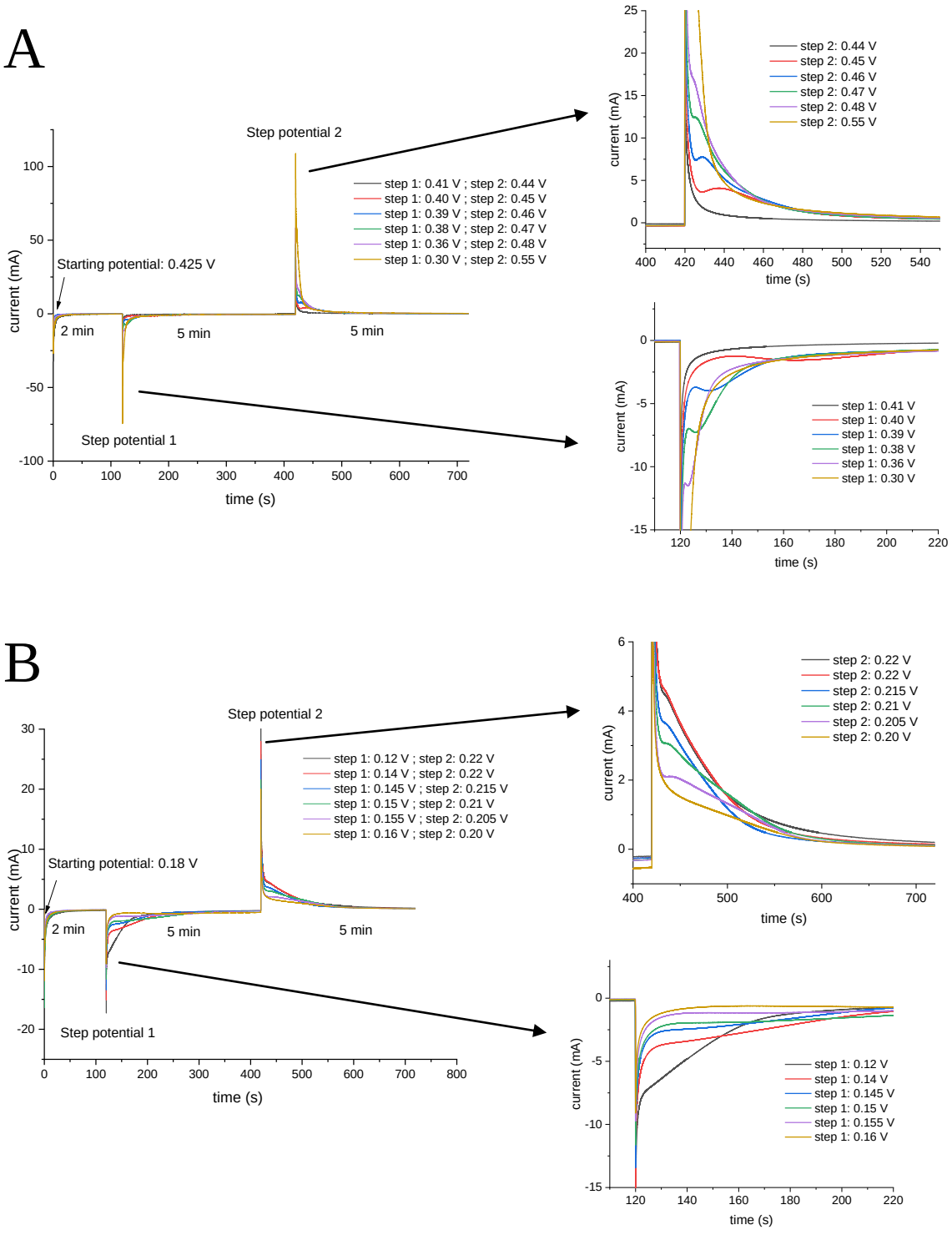

Figure S2. Double-potential-step chronoamperograms recorded at chloranil electrodes in (A) 2 M HCl (pH ≈ -0.3) and (B) 2 M acetate buffer. The potential (*vs.* SCE) was stepped first from open-circuit to (A) +0.425 V or (B) +0.180 V for 2 min, and then to the potentials 1 (see the legends for values) for 5 min, followed by the potentials 2 for 5 min.

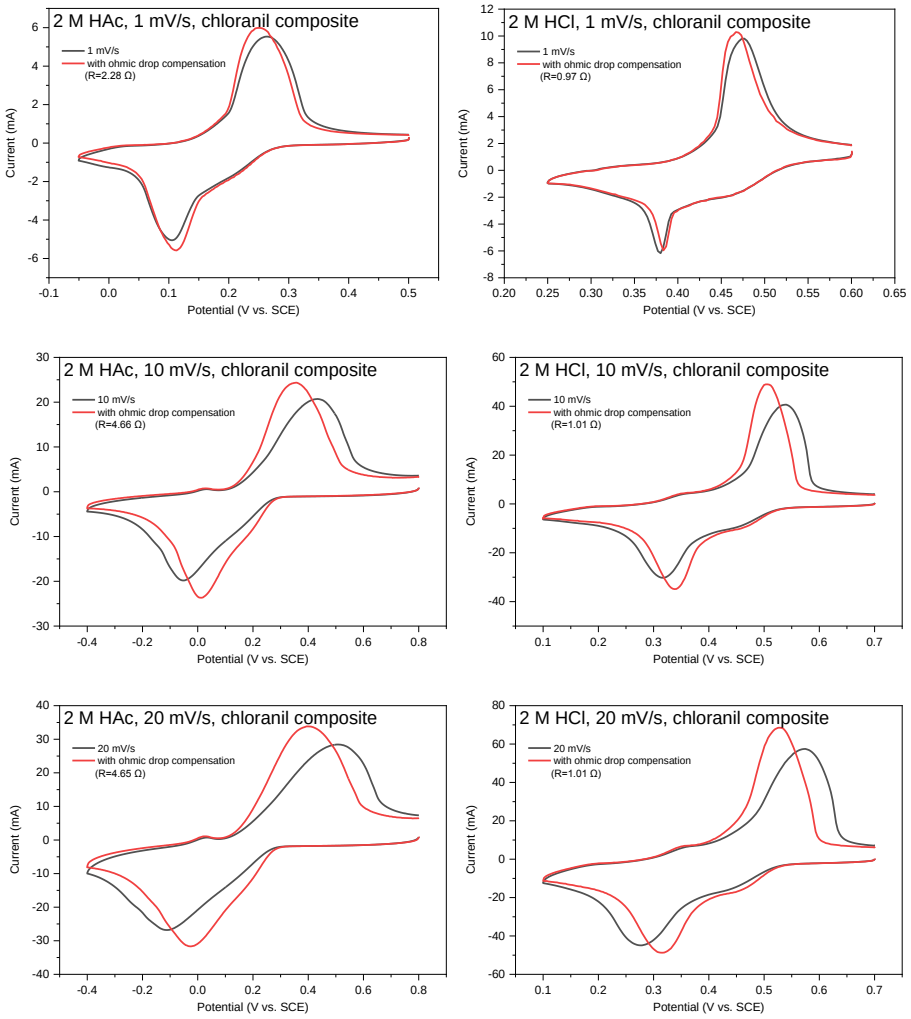

Figure S3. CVs of Ketjenblack EC-300J carbon-based chloranil electrodes recorded at different scan rates (the scan rates are reported on the graphs) in (left) a 2 M acetate buffer or (right) a 2 M HCl electrolyte, and (black) without and (red) with Ohmic drop compensation.

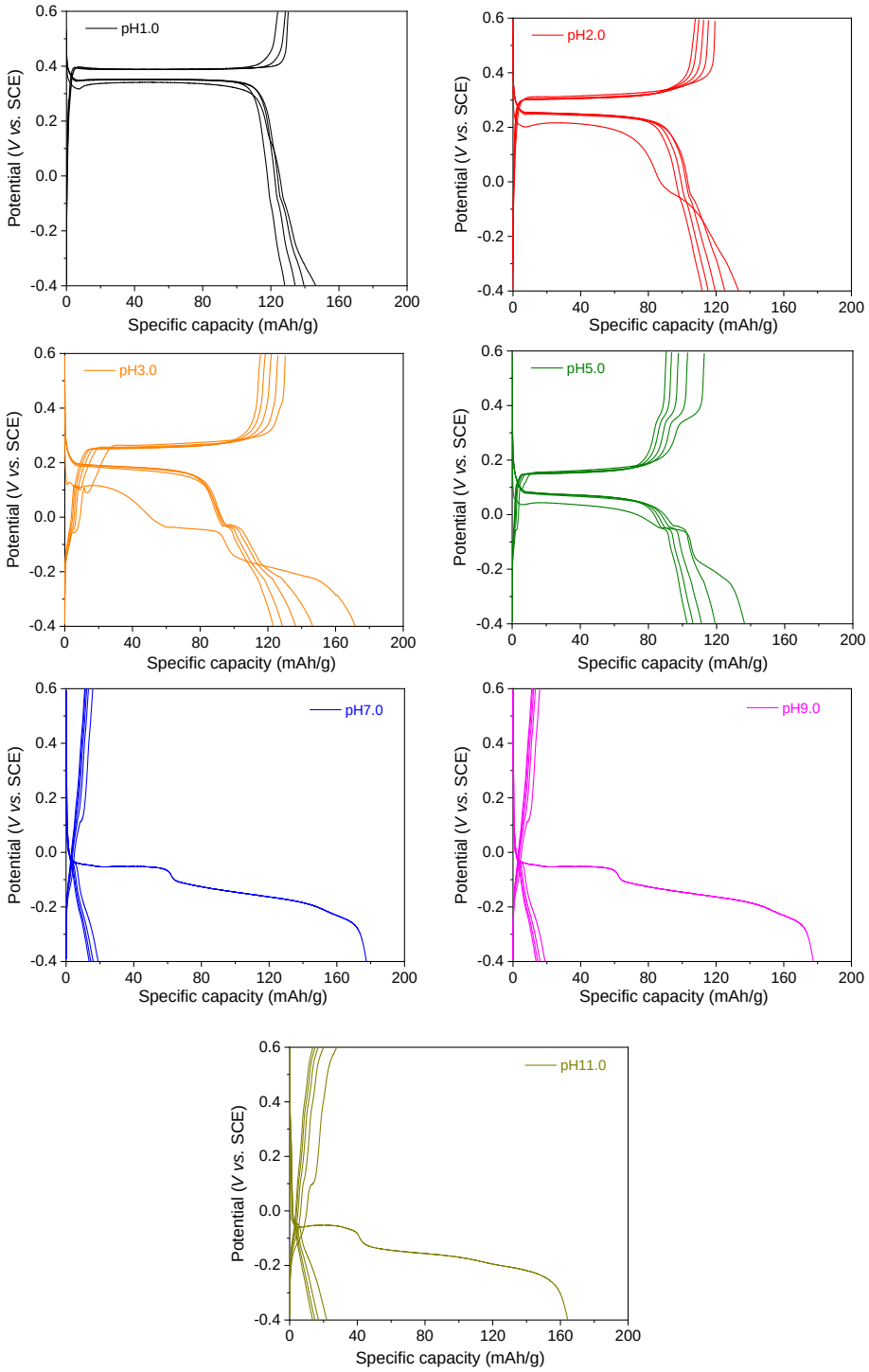

Figure S4. GDC cycling profiles (the first few cycles are shown) of Super P® carbon-based chloranil electrodes (rate: 0.5 mA/cm^2) in a set of buffered electrolytes at different pHs (the pH values are indicated on the graphs).

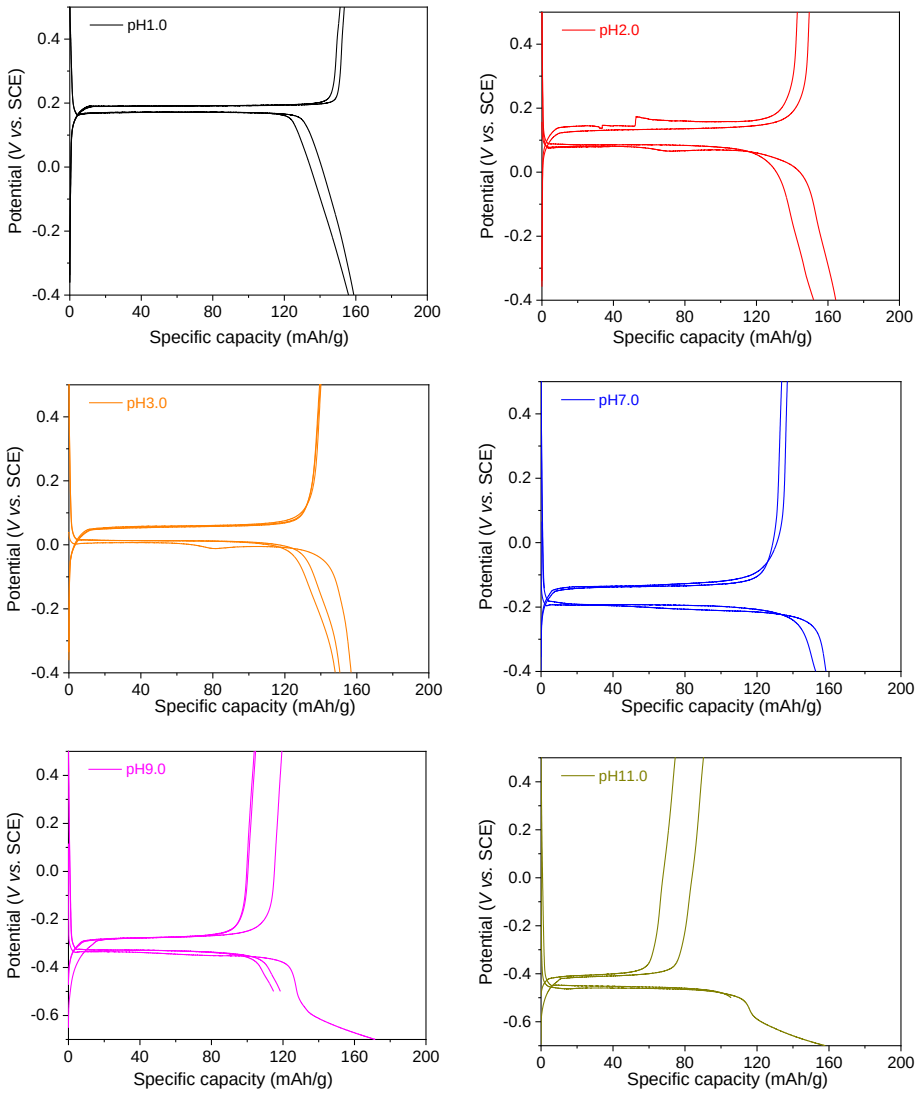

Figure S5. GDC cycling profiles (the first few cycles are shown) of Super P® carbon-based duroquinone electrodes (rate: 0.5 mA/cm^2) in a set of buffered electrolytes at different pHs (the pH values are indicated on the graphs).

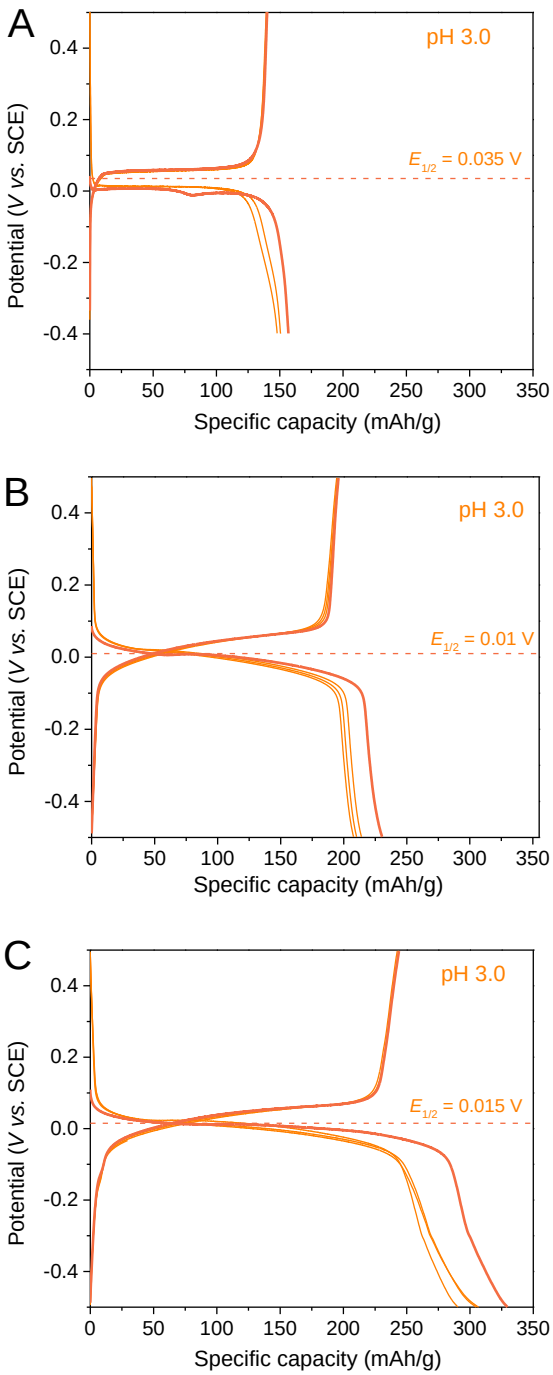

Figure S6. GDC cycling profiles (the first 3-4 cycles are shown and the first cycle is highlighted in bold) of (A) Super P® carbon-based, (B) Ketjenblack ED-300J carbon-based, and (C) Ketjenblack ED-600JD carbon-based duroquinone electrodes (rate: 0.5 mA/cm^2) in a 0.5 M chloroacetate buffer of pH 3.0.

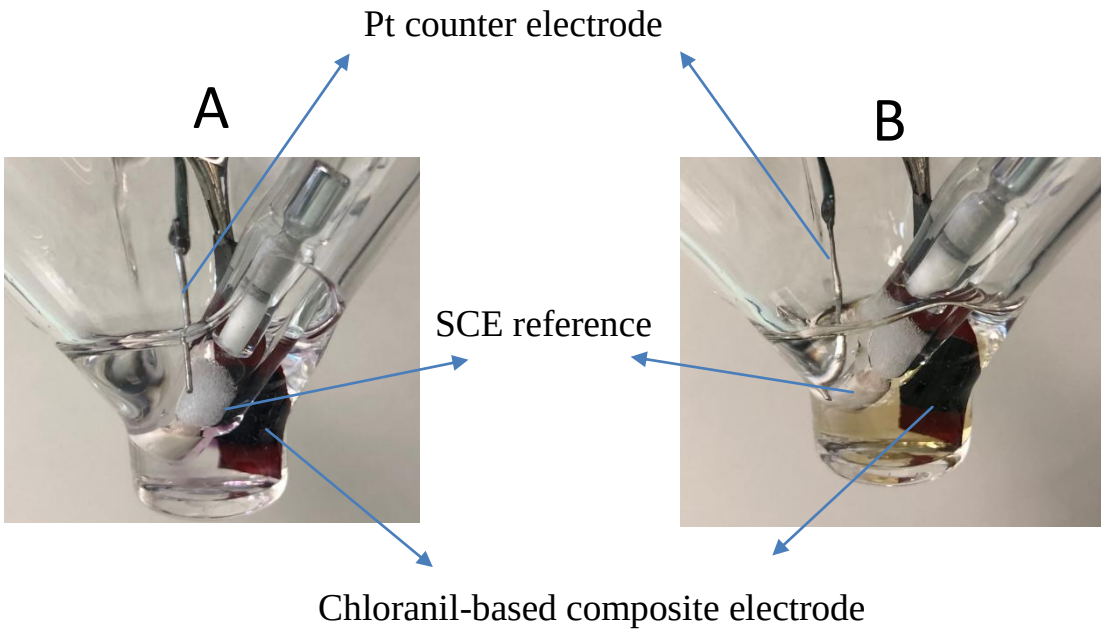

Figure S7. Pictures of the three-electrode cells after a first discharge/charge cycle (rate: 0.5 mA/cm^2) applied to a Ketjenblack carbon-based chloranil electrode immersed in (A) an acetate buffer of pH 5 or (B) a borate buffer of pH 7. In contrast to picture A, the appearance of a yellow color in the electrolyte of picture B indicates the presence of the reduced form of chloranil in the electrolyte.

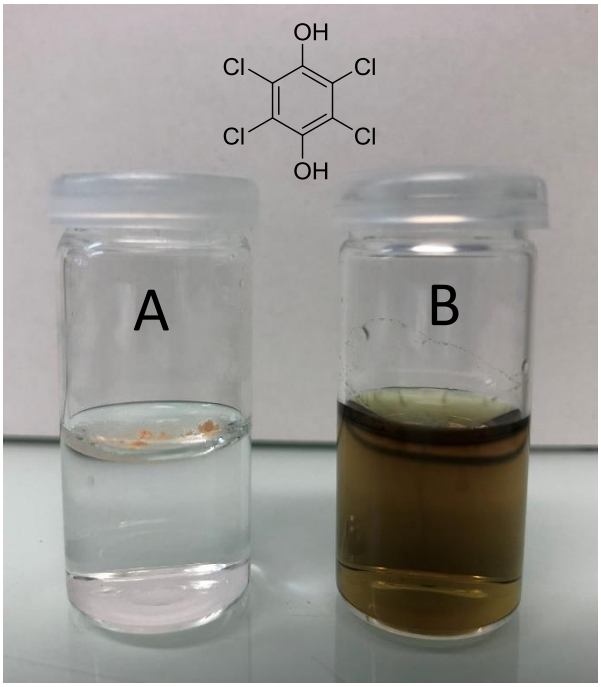

Figure S8. Picture of a 5 mL (A) acetate buffer at pH 5 and (B) borate buffer at pH 7 in which was added 10 mg of tetrachloro-1,4-hydroquinone. The hydroquinone is clearly insoluble at pH 5 (we can see the insoluble powder of tetrachloro-1,4-hydroquinone floating on the surface of water) but highly soluble at pH 7 (the hydroquinone dissolves spontaneously, turning the solution yellow-brown).

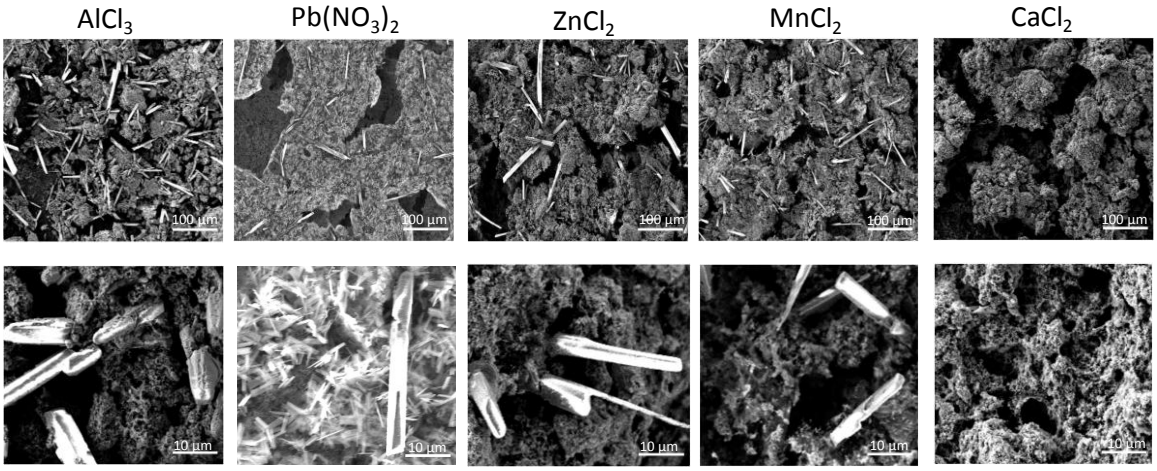

Figure S9. SEM images (top row: wide magnification; bottom row: closer magnification) of the surface of Ketjenblack EC-300J carbon-based chloranil electrodes (except for the $Pb(NO_3)_2$ SEM image which is the surface of a Super P® carbon-based chloranil electrode) after their first discharge in 0.5 M unbuffered electrolyte of $AlCl_3$, $Pb(NO_3)_2$, $ZnCl_2$, $MnCl_2$, and $CaCl_2$.

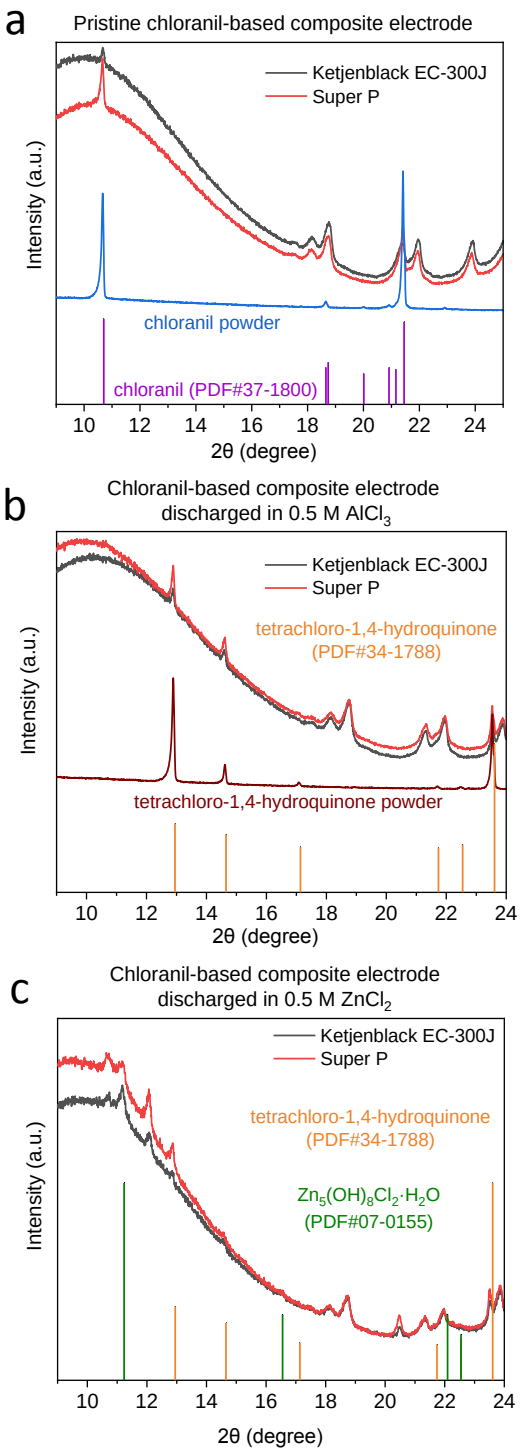

Figure S10. XRD patterns of Super P®- and Ketjenblack EC-300J carbon-based chloranil electrodes: (a) pristine electrode, (b) after a first discharge in a 0.5 M $AlCl_3$ electrolyte, (c) after a first discharge in a 0.5 M $ZnCl_2$ electrolyte. The theoretical and experimental XRD patterns of chloranil and tetrachloro-1,4-hydroquinone powders are also shown for comparison. In (c) the theoretical pattern of $Zn_5(OH)_8Cl_2 \bullet H_2O$ is included.

Table S1. Set of parameters used in the one-compartment 1D model to simulate the CVs reported in Figures 1 and 4.

	Parameters	Numerical values
Electrolyte compartment	$D_{A^-} = D_{AH}$ ($cm^2 \cdot s^{-1}$)	8×10^{-6} [a]
	$D_Q = D_{Q^{\bullet -}} = D_{QH^{\bullet}} = D_{Q^{2-}} = D_{QH^-} = D_{QH_2} = D_{QH_2^{\bullet +}}$ ($cm^2 \cdot s^{-1}$)	3.5×10^{-6}
	$D_{H_3O^+}$ ($cm^2 \cdot s^{-1}$)	9.5×10^{-5} S2, S3
	D_{OH^-} ($cm^2 \cdot s^{-1}$)	5.3×10^{-5} S4
	$k_{i,p} = k_{AH,p} = k_{w,p}$ ($M^{-1} \cdot s^{-1}$)	10^{10}
	k_i or k_{-i} ($M^{-1} \cdot s^{-1}$), depending on $K_{eq,i}$ [b]	10^9
	$k_{dis,i}$ or $k_{co,i}$ ($M^{-1} \cdot s^{-1}$), depending on $K_{dis,i}$ [b]	10^8
Interfacial electron transfer reactions	For duroquinone : $k_1^0 = k_2^0$ ($cm \cdot s^{-1}$)	1
	k_3^0 ($cm \cdot s^{-1}$)	300
	k_4^0 ($cm \cdot s^{-1}$)	30
	k_6^0 ($cm \cdot s^{-1}$)	2
	For chloranil : $k_1^0 = k_2^0 = k_3^0 = k_4^0 = k_6^0$ ($cm \cdot s^{-1}$)	1
	$\alpha_1 = \alpha_2 = \alpha_3 = \alpha_4 = \alpha_6$	0.5
Capacitance	C_{dl} ($\mu F \cdot cm^{-2}$)	30

[a] This value was selected for all added proton donors and proton acceptors in the electrolytes. It corresponds to an average diffusion coefficient value.

[b] See page S7 of SI for details.

Table S2. Set of parameters used in the two-compartment 1D model to simulate the GDCs reported in Figure 8.

	Parameters	Numerical values
Electrolyte compartment	$D_{A^-} = D_{AH}$ ($cm^2 \cdot s^{-1}$)	8×10^{-6}
	$D_{Q^{2-}} = D_{QH^-}$ ($cm^2 \cdot s^{-1}$)	3.5×10^{-6}
	$D_{H_3O^+}$ ($cm^2 \cdot s^{-1}$)	9.5×10^{-5}
	D_{OH^-} ($cm^2 \cdot s^{-1}$)	5.3×10^{-5}
	$k_{i,p} = k_{AH,p} = k_{w,p}$ ($M^{-1} \cdot s^{-1}$)	10^{10}-10^{11}
	k_i or k_{-i} ($M^{-1} \cdot s^{-1}$), depending on $K_{eq,i}$	10^9
Electrode compartment	$D_{A^-} = D_{AH}$ ($cm^2 \cdot s^{-1}$)	2.7×10^{-6}
	$D_Q = D_{Q^{\bullet -}} = D_{QH^\bullet} = D_{Q^{2-}} = D_{QH^-} = D_{QH_2} = D_{QH_2^{\bullet +}}$ ($cm^2 \cdot s^{-1}$)	10^{-4}
	$D_{H_3O^+}$ ($cm^2 \cdot s^{-1}$)	3×10^{-5}
	D_{OH^-} ($cm^2 \cdot s^{-1}$)	1.8×10^{-5}
	$k_{i,p} = k_{AH,p} = k_{w,p}$ ($M^{-1} \cdot s^{-1}$)	10^{10}-10^{11}
	k_i or k_{-i} ($M^{-1} \cdot s^{-1}$), depending on $K_{eq,i}$ [b]	10^9
	$k_{dis,i}$ or $k_{co,i}$ ($M^{-1} \cdot s^{-1}$), depending on $K_{dis,i}$ [b]	10^8
Electrode/ electrolyte interface	$P_{AH} = P_{A^-} = P_{H_3O^+} = P_{OH^-} = P_{Q^{2-}} = P_{QH^-}$	1[a]
	$k_{on,AH} = k_{on,A^-} = k_{on,H_3O^+} = k_{on,OH^-} = k_{off,i} = k_{on,i} / P_i$	0.1
	k_{off,QH^-} (s^{-1})	0.0001
	$k_{off,Q^{2-}}$ (s^{-1})	0.1
Interfacial electron transfer reactions	For duroquinone : $k_1^0 = k_2^0$ ($cm \cdot s^{-1}$)	1
	k_3^0 ($cm \cdot s^{-1}$)	300
	k_4^0 ($cm \cdot s^{-1}$)	30

	k_6^0 (cm·s^{-1}) For chloranil : $k_1^0 = k_2^0 = k_3^0 = k_4^0 = k_6^0$ (cm·s^{-1}) $\alpha_1 = \alpha_2 = \alpha_3 = \alpha_4 = \alpha_6$	2 1 0.5
Capacitance	C_{dl} (μF·cm^{-2})	10^5

[a] Partitioning coefficient of the subscript species i

References

(S1) N. Makivić, K. D. Harris, J-M. Tarascon, B. Limoges, V. Balland, *Adv. Energ. Mater.*, **2023**, *3*, 2203122.
(S2) V. Grozovski, S. Vesztergom, G. G. Láng, P. Broekmann, *J. Electrochem. Soc.*, **2017**, *164*, E3171–E3178.
(S3) H. L. Song, C. R. Jayendran, *J. Chem. Phys.*, **2011**, *135*, 124505.
(S4) E. L. Littauer, K. C. Tsai, *Electrochim. Acta*, **1979**, *24*, 351–355.